ARTICLE IN PRESS

Nature Communications

https://doi.org/10.1038/s41467-026-71061-3

Article in Press

A molecular switch in NAC prevents mitochondrial protein mistargeting by SRP

Received: 29 July 2025

Accepted: 9 March 2026

Cite this article as: Maldosevic, E., Gora, R.J., Lin, L.L. *et al.* A molecular switch in NAC prevents mitochondrial protein mistargeting by SRP. *Nat Commun* (2026). https://doi.org/10.1038/s41467-026-71061-3

Emir Maldosevic, Radoslaw Jakub Gora, Liangguang Leo Lin, Linyao Elina Zhou, Zexin Jason Li, Yelena Peskova, Ling Qi, Shu-ou Shan & Ahmad Jomaa

We are providing an unedited version of this manuscript to give early access to its findings. Before final publication, the manuscript will undergo further editing. Please note there may be errors present which affect the content, and all legal disclaimers apply.

If this paper is publishing under a Transparent Peer Review model then Peer Review reports will publish with the final article.

ARTICLE IN PRESS

© The Author(s) 2026. **Open Access** This article is licensed under a Creative Commons Attribution-NonCommercial-NoDerivatives 4.0 International License, which permits any non-commercial use, sharing, distribution and reproduction in any medium or format, as long as you give appropriate credit to the original author(s) and the source, provide a link to the Creative Commons licence, and indicate if you modified the licensed material. You do not have permission under this licence to share adapted material derived from this article or parts of it. The images or other third party material in this article are included in the article's Creative Commons licence, unless indicated otherwise in a credit line to the material. If material is not included in the article's Creative Commons licence and your intended use is not permitted by statutory regulation or exceeds the permitted use, you will need to obtain permission directly from the copyright holder. To view a copy of this licence, visit http://creativecommons.org/licenses/by-nc-nd/4.0/.

ARTICLE IN PRESS

A molecular switch in NAC prevents mitochondrial protein mistargeting by SRP

Authors

Emir Maldosevic[1,5], Radoslaw Gora[2,5], Liangguang Leo Lin[1], Linyao Elina Zhou[1], Zexin Jason Li[1,3], Yelena Peskova[1], Ling Qi[1], Shu-ou Shan[2*], and Ahmad Jomaa[1,4*]

Affiliations

[1]Department of Molecular Physiology and Biological Physics, University of Virginia, Charlottesville, VA 22903, USA

[2]Division of Chemistry and Chemical Engineering, Caltech, Pasadena, CA 91125, USA

[3]Medical Scientist Training Program, University of Virginia, School of Medicine, Charlottesville, VA 22903, USA

[4]Department of Biochemistry and Molecular Genetics, University of Virginia, Charlottesville, VA 22903, USA

[5]These authors contributed equally to this work

[*]**Corresponding authors:** ahmadjomaa@virginia.edu, and sshan@caltech.edu

ARTICLE IN PRESS

ARTICLE IN PRESS

Abstract

The nascent polypeptide-associated complex (NAC) co-translationally screens all nascent proteins and regulates their access to the signal recognition particle (SRP) to ensure the fidelity of protein targeting to the endoplasmic reticulum (ER). However, the mechanism by which NAC prevents the mistargeting of nascent mitochondrial proteins remains unclear. Here, we identify a molecular switch in NAC that allows its central barrel domain to adopt a stabilized conformation on ribosomes exposing a mitochondrial targeting sequence (MTS). Mutations of the MTS on the nascent chain or in the NAC switch region increase NAC barrel dynamics and reduce its binding to the ribosome. This leads to an impaired ability of NAC to prevent mistargeting by SRP and causes ER stress in human cells. Our work reveals how NAC detects nascent mitochondrial proteins early in translation and prevents their promiscuous access to SRP, elucidating the structural basis that underlies this role and providing mechanistic insights into protein targeting fidelity with broader implications for cellular proteostasis.

ARTICLE IN PRESS

Introduction

During protein synthesis, nascent polypeptides are co-translationally sorted to distinct cellular destinations, a process critical for maintaining protein homeostasis[1,2]. This process begins on the ribosome, where the nascent polypeptide-associated complex (NAC) binds and screens all emerging nascent chains to regulate their localization and processing[3,4]. The majority of mitochondrial proteins are nuclear-encoded and synthesized in the cytosol[5–7] where they must be properly screened by NAC to ensure accurate targeting. As part of this screening, nascent chain access to targeting factors, such as the signal recognition particle (SRP) that delivers translating ribosomes to the endoplasmic reticulum (ER), must be tightly controlled by NAC to prevent the mistargeting of mitochondrial proteins[8]. Despite its critical role in nascent chain sorting, whether and how NAC detects nascent mitochondrial precursor proteins and distinguishes them from ER-targeted proteins remain unclear.

NAC is an essential and conserved ribosome-associated complex in eukaryotes[9–11] that is expressed at equimolar levels to ribosomes[12]. It is composed of the NACα and NACβ subunits[13], which dimerize to form a central β-barrel domain[14,15]. NACβ anchors the complex to the ribosome with nanomolar affinity[16] using a basic N-terminal tail that interacts with both ribosomal proteins and ribosomal RNA (rRNA)[17–19]. Previously, AlphaFold models fitted into lower resolution cryo-EM densities (~6-8 Å) suggested that two amphipathic helices (βh2 and αh1) in the NAC barrel domain lock together to form a clasp coordinated by a series of hydrophobic residues[19] which mediate binding of the barrel domain near the polypeptide exit tunnel[17,18]. This positions the barrel domain to potentially interact with nascent chains emerging from the exit tunnel[20,21] and coordinate their co-translational processing[22–28] or targeting[19,29,30].

ARTICLE IN PRESS

ARTICLE IN PRESS

One of the best-established functions of NAC is to prevent the mistargeting of nascent proteins to the ER[8] by regulating the interaction, conformation, and activity of SRP[16,19,29–31]. SRP contains an M-domain, which recognizes an N-terminal hydrophobic ER targeting signal on nascent proteins emerging from the ribosome, and a GTPase NG-domain that dimerizes with the SRP receptor (SR) at the ER membrane[16,29,32]. Engagement of the M-domain with the signal sequence activates SRP for rapid assembly with SR to turn on ER targeting[33,34] and prevents ER proteins from being mistargeted to mitochondria[35]. However, the specificity of ribosome binding and activation of SRP and SR is limited[13,16]. NAC uses dual mechanisms to regulate ER targeting. A flexibly tethered C-terminal UBA domain in NACα recruits SRP to translating ribosomes[19], whereas the NAC barrel domain prevents the promiscuous activation of SRP by blocking the access of the SRP M-domain to the ribosome exit tunnel[8,29,30]. When an ER signal sequence emerges from the ribosome, the NAC barrel becomes destabilized, allowing SRP to displace it from the ribosome tunnel exit so that the nascent chain can be accurately targeted to the ER[19]. Unlike ER proteins, mitochondrial proteins do not destabilize NAC binding to the ribosome[19]. Thus, the specificity of nascent chain sorting by NAC is crucial to prevent mitochondrial protein mistargeting to the ER[8].

ARTICLE IN PRESS

A significant subset of mitochondrial proteins contain an N-terminal mitochondrial targeting sequence (MTS) that allows for their proper subcellular localization[36,37]. An MTS is a bipartite sequence motif characterized by clusters of positively charged residues on the polar face of a short amphipathic helix followed by a disordered sequence of 20-90 amino acids. The MTS, in particular the N-terminal basic amphiphilic helix, is recognized by receptors and the translocase at the outer mitochondrial membrane (TOM) and is often necessary and sufficient to direct nascent mitochondrial proteins for targeting and import[6,7,38–40]. However, whether NAC directly senses the

ARTICLE IN PRESS

MTS during translation prior to targeting and how NAC prevents promiscuous interactions of the MTS with SRP on the ribosome remains poorly understood.

Here, we determine the cryo-EM structure of human NAC bound to ribosomes translating a mitochondrial nascent chain with an N-terminal MTS. The structure reveals that the NAC barrel domain shifts to adopt a stabilized conformation docked at the rRNA helix H59 (H59-docked state) near the polypeptide exit tunnel mediated by a distinct set of ribosomal contacts that are distinct from previous observations of NAC bound to ribosomes translating an ER signal sequence or a cytosolic protein[19,22,23]. We identify a molecular switch in NACβ that allows NAC to alternate between different conformations. Single-molecule studies and biochemical assays indicate that mutations of the MTS disrupt the anchoring of the NAC barrel domain at the ribosome exit site, leading to the promiscuous activation of SRP on ribosomes exposing a nascent mitochondrial protein. Finally, we show that mutations in the NAC switch region fail to rescue to ER stress phenotypes that are associated with protein mistargeting in human cells. Our work uncovers a previously unappreciated ability of NAC to sense an MTS early during translation and the molecular mechanism employed by structural elements within NAC to prevent the mistargeting of nascent mitochondrial proteins.

Results

The NAC barrel adopts a distinct conformation on ribosomes translating an MTS

Previous studies established that NAC mediates proper protein sorting by preventing SRP access to ribosomes that do not carry signal sequences[8,19,29]. To first confirm if NAC deletion leads to mitochondrial protein mislocalization in human cells, *NACβ* knockout (KO) HEK293T cells were generated using CRISPR-Cas9 (Supplementary Fig. 1A). Immunofluorescence staining was

ARTICLE IN PRESS

ARTICLE IN PRESS

conducted to assess the localization of OXA1L and HSP60, which are targeted to the inner mitochondrial membrane and mitochondrial matrix, respectively. In wild-type (WT) cells, both HSP60 and OXA1L co-localized with the mitochondrial marker TOM20 (Supplementary Fig. 1B-C). In contrast, *NACβ*-KO cells showed mislocalization of both proteins, with fluorescence signals accumulating outside mitochondria, indicating impaired mitochondrial protein sorting in the absence of NACβ.

Next, we asked how NAC engages with ribosomes carrying an MTS. Model MTS-containing nascent chains derived from OXA1L and HSP60 were generated by stalling ribosomes during translation with the XBP1 arrest peptide[41] or on mRNA lacking a stop codon[42], respectively. NAC was added to salt-washed stalled ribosome-nascent chain complexes (RNCs), exposing the N-terminal MTS (RNC_{MTS}) of OXA1L (74 residues) or HSP60 (62 residues), to obtain a homogeneous population suitable for structural analysis. As a control, an MTS deletion mutant of OXA1L was also purified (Supplementary Fig. 2). Single particle cryo-EM analysis was used to visualize the interactions between NAC and ribosomes translating mitochondrial nascent chains (Supplementary Table 1).

ARTICLE IN PRESS

Initial 2D and 3D classifications yielded heterogenous 80S particles with different translation states. Further iterative 3D variability analyses were conducted using focused masks to sort for ribosomes translating mitochondrial nascent chains, which resulted in a final set of particles containing density for P-site tRNA, nascent chain, and NAC (Supplementary Fig. 3A-B, Supplementary Fig. 4A-B). The cryo-EM structures of both OXA1L- and HSP60-RNC_{MTS} resolved NAC bound next to the polypeptide exit tunnel. The overall resolution of the two maps was ~2.6 Å and ~3.0 Å. NAC was resolved between 3-6 Å (Supplementary Fig. 3C-D,

Supplementary Fig. 4C-D) in a similar conformation on the ribosome for both MTS constructs interacting with rRNA helix 59, termed the H59-docked state (Supplementary Fig. 5A-C). Since the NAC barrel domain was better resolved in the OXA1L-RNC$_{MTS}$ map, this map was used for further interpretation of the structure.

The NAC barrel was docked near the polypeptide exit tunnel (red asterisk, Fig. 1A), consistent with its role in protecting and scanning emerging nascent chains[8,21]. Cryo-EM density corresponding to the nascent chain was present in the polypeptide exit tunnel, but the nascent chain including the MTS was not resolved outside the ribosome due to flexibility (Fig. 1A, Supplementary Fig. 6A-B). In the current H59-docked state, NAC was stabilized by a series of contacts between NACβ and the ribosome (Fig. 1B-E) that were not previously observed in the structure of NAC bound to ribosomes translating an ER signal sequence (RNC$_{SS}$)[19].

NACβ contains a conserved N-terminal RRKKK motif, which is essential for high-affinity ribosome binding of the complex[17]. This ribosome 'anchor' of NAC was previously observed to intercalate around the C-terminal tail of eL22, forming extensive interactions between the ribosomal RNA (rRNA) and the ribosomal protein eL19[19]. In addition to the previously observed ribosome contacts, we resolved an additional insertion of the first 4 N-terminal residues of NACβ wedged between rRNA helix 59 (H59) and eL22, which forms the fluke of the NAC anchor (Fig. 1C, Supplementary Fig. 7A-B). A combination of polar and stacking interactions mediate the contacts with eL22, consistent with crosslinking data[21].

These previously unresolved contacts are established following a large conformational shift of the NAC barrel towards H59 (colored grey vs. white, Fig. 1F). In particular, the base of the barrel that

ARTICLE IN PRESS

directly contacts the ribosome moves by 10 Å away from the polypeptide exit tunnel. To accommodate this shift, H59 undergoes a conformational change where it lifts away from the ribosome by 9 Å (red arrows, Fig. 1F). In this state, the rRNA bases G2706 and U2707 are flipped out following rearrangement of the rRNA (red arrows, Fig. 1G) allowing NAC to dock at rRNA H59.

Two predicted amphipathic helices in the NAC barrel domain (βh2 and αh1) and part of the linker on NACβ that connects the barrel domain to the anchor (Fig. 1B) were resolved at side-chain resolution and built *de novo* (Fig. 1D and Supplementary Fig. 8A-C). These amphipathic helices form a clasp containing a hydrophobic core (Supplementary Fig. 8A) and mediate the interactions (described below) that stabilize the NAC barrel on the ribosome. The H59-docked state is distinct from previous structures of NAC bound to ribosomes translating and displaying an ER signal sequence (H59-undocked state), in which NAC is further away from H59 and both the hydrophobic clasp and contacts with the ribosome were destabilized by the emergence of a signal sequence and thus were not well resolved[19].

ARTICLE IN PRESS

A molecular switch regulates NAC binding to the ribosome

Several residues in NAC βh2 and the preceding linker, conserved among higher eukaryotic organisms, were identified as mediating interactions with the ribosome (Fig. 2A). In the NACβ linker region, His34 inserts below H59 to lock NAC in a stable conformation on the ribosome (Fig. 2A), while the side chain of Arg35 interacts with the flexible C-tail of eL22 (Fig. 2B and Supplementary Fig. 8A). Furthermore, Lys42 is within range for electrostatic interactions with the phosphate backbone of rRNA H59, while Phe46 stacks with Asn34 on eL19 (Fig. 1E, Supplementary Fig. 8C). These interactions are formed in the H59-docked state of the RNC_{MTS}

ARTICLE IN PRESS

structure following a conformational change in the NAC βh2 and the preceding linker, when compared to the previous RNC_{SS} structure (Fig. 2B).

To investigate the role of these previously uncharacterized contacts in ribosome binding, residues mediating NAC barrel domain interactions with the ribosome (His34, Arg35, Lys42, and Phe46) were mutated to either Glu/E or Ala/A and purified (Supplementary Fig. 9A-B). We tested the ability of the NAC mutants to interact with human ribosomes isolated from HEK293 cells using an *in vitro* co-sedimentation assay. Both single and double mutations in the NACβ linker (His34 and Arg35) and the amphipathic helix βh2 (Lys42 and Phe46) significantly reduced NAC association with ribosomes when compared to wild-type (WT) NAC (Fig. 2C-D, Supplementary Fig. 9C-D).

Together, our structural and biochemical data reveal a molecular switch within NACβ that undergoes a conformational change involving the linker residues (His34 and Arg35) and the amphipathic helix βh2. Upon binding ribosomes displaying an MTS, this switch engages with rRNA helix H59 and stabilizes the positioning of the NAC barrel near the polypeptide exit tunnel.

ARTICLE IN PRESS

The molecular switch alters NAC barrel dynamics on the ribosome

We next directly assessed how contacts of the switch region (Fig. 3A) influence NAC conformations on the ribosome by conducting single-molecule total internal reflection fluorescence microscopy (smTIRFM) studies using OXA1L RNC_{MTS} immobilized on a glass coverslip surface (Fig. 3B). This approach selectively monitors populations of WT or mutant NAC that are bound to surface-immobilized ribosomes and excludes unbound NAC.

ARTICLE IN PRESS

The position of the NAC barrel at the ribosome tunnel exit was measured by Förster resonance energy transfer (FRET) between a donor dye (Cy3B) on the NAC barrel domain and an acceptor dye (Atto647N) incorporated at residue 39 in the OXA1L nascent chain. This residue is 35 amino acids from the C-terminus of the nascent chain and places the dye at the polypeptide exit tunnel (Fig. 3B). Hidden Markov modeling (HMM) of the fluorescence time traces showed dynamic transitions of the NAC barrel between three states, with low, medium, and high FRET efficiency, on the second timescale (Fig. 3C). The majority of WT NAC displayed long-lived high FRET traces with brief transitions to medium and low FRET states (Fig. 3C), indicating stable docking of the barrel in close proximity to the tunnel exit. In contrast, NAC bearing mutations in the NACβ linker (HR:AA) or βh2 (KF:AA) more frequently sampled the medium and low FRET states (Fig. 3C). These differences are reflected in the FRET histograms, which show that WT NAC resides primarily in the high FRET state, whereas the FRET distribution for NAC switch mutants shifted to medium- and low-FRET states (Fig. 3D-E). These results demonstrate that the docking of the NAC barrel at the ribosome tunnel exit was impaired by mutations in the switch region.

ARTICLE IN PRESS

We further measured the kinetic stability of NAC interactions with RNC_{MTS} using smTIRFM. Over 80% of WT NAC dissociated from RNC_{MTS} with a rate constant of ~0.14 s^{-1}, while the remainder dissociated at a faster rate (Supplementary Fig. 10A). The more-stably bound population (slow-dissociating) decreased to ~40% and ~20%, respectively, with NAC mutants HR:AA and KF:AA (Supplementary Fig. 10B). Thus, mutations in the NAC switch region impaired proper barrel docking on the ribosome surface, and the faster dissociation of these mutants compared to WT NAC are consistent with co-sedimentation assays showing reduced mutant binding to ribosomes (Fig. 2C-D). We note that despite the weakened binding, the association of HR:AA and KF:AA were still confidently detected under smTIRFM with < 5 nM NAC present, indicating that both

ARTICLE IN PRESS

NAC mutants still bind ribosomes with high affinity. Taken together, these data suggest that the molecular switch controls the conformational dynamics of the NAC barrel on the ribosome.

MTS mutations destabilize the NAC barrel on the ribosome

We next asked whether the stabilized conformation of the NAC barrel domain in the H59-docked state at the ribosome exit site is influenced by the presence of an MTS. To this end, we either deleted the amphiphilic helical segment of the MTS in the OXA1L nascent chain ($OXA1L_{\Delta MTS}$) or replaced this region with the ER signal sequence from a bona fide SRP substrate preprolactin ($OXA1L_{MTS\text{-}to\text{-}SS}$) (Fig. 4A). smTIRFM experiments were performed to monitor the NAC barrel conformation on RNCs carrying the mutated MTS. Both mutations led to increased dynamics of the NAC barrel, substantially increasing the population in low and medium FRET states compared to that on RNC bearing the WT OXA1L MTS (Fig. 4B-C). In addition, the more stably bound (slow-dissociating) NAC population on these RNCs decreased to ~40% and ~60% for the $OXA1L_{\Delta MTS}$ and $OXA1L_{MTS\text{-}to\text{-}SS}$ nascent chain, respectively, compared to 80% on $OXA1L_{WT}$ (Fig. 4D-E).

Based on the smFRET data, we hypothesized that mutation of the MTS destabilizes the NAC barrel, similar to previous structures of NAC bound to ribosomes displaying the nascent chain of an SRP substrate, preprolactin[19]. We therefore determined the structure of NAC bound to ribosomes translating $OXA1L_{\Delta MTS}$ (Supplementary Fig. 11A-D). A 3D variability analysis of the $OXA1L_{\Delta MTS}$ dataset similar to that performed for the MTS dataset revealed multiple NAC classes exhibiting barrel movements on the ribosome (Fig. 4F, Supplementary Fig. 12A-B). In addition to the H59-docked state, we observed the H59-undocked state similar to a previous structure of NAC on ribosomes translating an ER substrate[19] where the barrel moves away from H59 and towards

ARTICLE IN PRESS

the polypeptide exit tunnel (Supplementary Fig. 13A-C). This state showed less-defined EM-densities for the two amphipathic helices of NAC implying increased dynamics in this region, consistent with previous observations[19]. Collectively, these results indicate that the H59-docked state is promoted by the presence of an MTS which is likely crucial for preventing improper targeting of MTS-containing nascent chains by SRP.

NAC mutants fail to regulate SRP conformation on RNCs

We next tested whether the contacts made by the NAC switch region are important for preventing the mistargeting of ribosomes exposing a nascent MTS. SRP is activated for ER targeting when the SRP54 M-domain engages the ER signal sequence emerging from the exit tunnel, which induces SRP to adopt a 'Proximal' conformation in which the SRP54 NG-domain docks at uL23 and optimally associates with the SRP receptor at the ER[16,34]. Previously, we showed that NAC blocks SRP from adopting the targeting-active proximal conformation on ribosomes lacking an ER targeting signal and thus prevents mistargeting[16]. In the current conformation of NAC on RNC_{MTS}, the NAC barrel is stabilized at the exit tunnel and would effectively block the binding of SRP54 M-domain at the exit tunnel (Fig. 5A), thus preventing the activation of SRP[16,32]. We hypothesize that the loss of the molecular switch would impair this sorting function of NAC, by reducing the stable docking of the NAC barrel at the polypeptide exit tunnel.

ARTICLE IN PRESS

We conducted smTIRFM experiments to observe the conformational dynamics of SRP bound to ribosomes translating either an ER or a mitochondrial nascent chain. The proximal conformation of SRP was detected using FRET between a donor dye (Atto550) and an acceptor dye (Atto647N) labeled on SRP19 and SRP54, respectively (Fig. 5B)[16,43]. On ribosome bearing an ER signal sequence from preprolactin, SRP is dominated by a high FRET state that reports on the proximal

conformation, both in the absence and presence of NAC (Fig. 5C), consistent with previous results[16]. On ribosomes exposing the MTS of OXA1L, SRP is distributed between three conformations, with ~40% of SRP in the high-FRET, proximal conformation that is targeting-active (Fig. 5D). The proximal conformation of SRP on RNC_{MTS} was abolished by WT NAC, whereas both NAC mutants failed to regulate the conformation of SRP (Fig. 5D-E). Thus, mutations in the switch region abolished the ability of NAC to prevent the mis-activation of SRP on ribosomes translating an MTS.

Previous work demonstrated that *NAC* knockdown led to the mistargeting of mitochondrial proteins to the ER, which induced modest ER stress and elevated expression of ER chaperones BiP and PDI[8]. We therefore tested the importance of the NAC molecular switch in preventing protein mistargeting to the ER by assessing the levels of ER chaperones and the splicing of the *XBP1* mRNA, both of which report on ER stress[44,45]. We first showed that *NACβ*-KO HEK293T cells displayed increased levels of the ER chaperones, BiP and PDI (Supplementary Fig. 14A), as well as *XBP1* mRNA splicing (Supplementary Fig. 14B). We then reintroduced either WT or mutant NACβ in the *NACβ*-KO cells. Overexpression of WT NACβ partially restored the ER stress markers, while both the NACβ HR:AA and KF:AA mutants failed to rescue the ER stress phenotype (Fig. 5F-G).

To assess whether ER stress in *NACβ*-KO cells arises from mistargeting of mitochondrial proteins to the ER where they become aberrantly glycosylated, we performed concanavalin A (ConA) pulldowns of glycosylated proteins from whole-cell lysates[8]. We observed a substantial increase in glycosylated HSP60 accumulation in *NACβ*-KO HEK293T cells relative to WT cells (Supplementary Fig. 15A-B). Overexpression of WT NACβ partially rescued glycosylated HSP60

ARTICLE IN PRESS

accumulation (0.3 for WT versus 0.5 for rescue compared to KO levels), whereas the NACβ switch mutants failed to rescue the phenotype to the same levels (1.4 for the NACβ HR mutant and 0.8 for the KF mutant). Taken together, our results indicate that the NAC molecular switch prevents non-specific binding and activation of SRP to MTS-containing RNCs, and when perturbed, can lead to mitochondrial protein mistargeting which induces modest ER stress in human cells.

Discussion

NAC is an essential protein biogenesis factor, conserved from yeast to humans, that interacts with all nascent chains[20,21] as they emerge from the ribosome to facilitate proper protein sorting and biogenesis[3]. Based on our results, we propose that NAC adopts a stabilized conformation near the polypeptide exit tunnel when engaging ribosomes translating an MTS. This H59-docked state of NAC is critical for preventing promiscuous SRP activation and ensures the correct sorting of mitochondrial proteins (Fig. 6). Either deletion of an MTS or mutations in the molecular switch increases NAC barrel dynamics, allowing SRP to adopt a targeting-active conformation that can lead to mistargeting of nascent proteins.

ARTICLE IN PRESS

Recent studies showed that H59 interacts with NAC, SRP[19], MAP1[23], MAP2[46], and the multi-functional protein EBP1[47]. Interestingly, the conformational change in H59 observed in the current structure and the subsequent repositioning of the barrel are different from previous reported structures, where either H59 or the NAC barrel clashes with the position of these associated factors (Supplementary Fig. 16A-C). Thus, the conformational landscape of H59 may serve as an additional regulatory element to enhance the specificity of nascent chain sorting, processing, and targeting on the ribosome during translation.

ARTICLE IN PRESS

Nascent chain properties such as hydrophobicity and secondary structural features are known to influence the interaction of NAC on the ribosome[16,19,20]. For example, hydrophobic ER signals weaken NAC binding on the ribosome, presumably by destabilizing the NAC barrel, to allow for SRP recruitment[19]. In contrast, both our structure and single-molecule experiments showed stable docking of the NAC barrel at H59 on ribosomes exposing an MTS. Deletion of the characteristic amphiphilic helix in the MTS or substitution of this helical element with an ER signal sequence impairs the stable docking of the NAC barrel. The absence of discernible density for the MTS in our cryo-EM maps suggests that its interaction with NAC is either highly transient or mediated through an allosteric effect that modulates NAC conformation and ribosome engagement. An alternative model is that NAC is displaced from the H59-docked conformation on ribosomes translating cytosolic or ER proteins due to direct interactions with the nascent chain. While our study focuses on elucidating the molecular mechanism by which NAC prevents SRP from accessing mitochondrial nascent chains via a molecular switch, how NAC engages with cytonuclear clients remains unresolved and requires further investigation.

ARTICLE IN PRESS

Mutagenesis experiments further demonstrate that the molecular switch plays a key role in stabilizing the H59-docked conformation of NAC on the ribosome, which is essential to prevent the non-specific recruitment and activation of SRP on ribosomes lacking an ER targeting signal[16]. Accordingly, NAC switch mutants fail to properly triage MTS-nascent chains, leading to the promiscuous activation of SRP on the ribosome. Furthermore, NAC mutants failed to fully rescue ER mistargeting and stress caused by the depletion of NAC in human cells. Thus, stable docking at the ribosome exit by the NAC barrel domain is critical to prevent the mistargeting of mitochondrial nascent chains to the ER.

ARTICLE IN PRESS

Our results provide additional evidence for the role of NAC as a molecular gatekeeper at the ribosome. The toggling of the NAC barrel domain on ribosomes, mediated by the NAC molecular switch, provides a critical mechanism explaining how NAC senses newly synthesized proteins and contributes to mitochondrial protein sorting in humans. Disruption of this switch can lead to protein mistargeting and cellular stress, highlighting the importance of the regulatory mechanisms employed by NAC in maintaining cellular proteostasis. Whether and how NAC facilitates ribosome recruitment to mitochondria remains an important unresolved question that requires future investigation.

ARTICLE IN PRESS

Methods

Immunofluorescence

HEK293T cells were cultured on Millicell EZ SLIDE 8-well chamber (Millipore # PEZGS0816) for 24 hours. The cells were fixed by 4% paraformaldehyde (PFA) for 10 minutes at room temperature, followed by three washes with PBS. The fixed cells were simultaneously incubated with primary antibodies in blocking buffer (0.3% donkey serum and 0.25% Triton X-100 in PBS) overnight at 4 °C. Following three washes with PBS, the samples were incubated with secondary antibodies for 2 hours at room temperature. Mounting was performed with mounting medium containing DAPI (Vector Laboratories, cat no. H-1200) and Fisherfinest Premium Cover Glasses (Fisher Scientific, cat no. 12-548-5P). Images were captured using the Zeiss LSM 980 confocal microscope at the University of Virginia Advanced Microscopy Facility. Antibodies for immunostaining were as follows: anti-HSP60 (mouse, Invitrogen, cat no. MA3-012, 1:200), anti-TOM20 (rabbit, Proteintech, cat no. 11802-1, 1:200), anti-OXA1L (rabbit, Proteintech, cat no. 21055-1, 1:200), anti-TOM20 (mouse, Abcam, cat no. ab56783, 1:200). Secondary antibodies for fluorescent immunostaining (all 1:500) were as follows: Anti-rabbit IgG Alexa Fluor 488 (Jackson

ImmunoResearch, cat no. 711-545-152), anti-Mouse IgG Alexa Fluor 555 (Invitrogen, cat no. A32773).

NAC Purification

A construct encoding for 6xHis-NACα and NACβ in a pET28b vector[22] was expressed in *E. coli* BL21-CodonPlus DE3 competent cells (Agilent, cat no. 230245). QuickChange (Agilent, cat no. 210518) site-directed point mutagenesis was conducted to generate mutations in NACβ. The following procedures were used to purify all NAC variants. Cells were grown to OD600 0.6-0.9 at 37 °C and induced with 1 mM IPTG at 18 °C overnight. Cells were pelleted, resuspended in 15 mL of lysis buffer (50 mM HEPES-KOH pH 7.5, 1M NaCl, 10% Glycerol, 6 mM β-mercaptoethanol, protease inhibitor (Roche, cOmplete mini, cat no.11836153001)), and lysed using a French press. The lysate was centrifuged using a TI 50.2 rotor at 20,000 rpm for 30 min at 4°C (2X). The supernatant was loaded on a 5 mL HisTrap HP column (Cytiva, cat no. 17524802) using a P1 pump at 4°C and washed with 1-2 column volumes (CV) of Nickel A buffer (50 mM HEPES-KOH pH 7.5, 1 M NaCl, 45 mM Imidazole, 10% glycerol, 6 mM β-mercaptoethanol). The column was transferred to an Akta Pure fast protein liquid chromatography system (Cytiva) and washed for an additional 5 CV in nickel A buffer. Purified proteins bound to the column were eluted in a step gradient using 2-3CV of 15% and 30% nickel B buffer (50 mM HEPES-KOH pH 7.5, 150 mM KOAc, 300 mM Imidazole, 10% glycerol, 6 mM β-mercaptoethanol).

Fractions from the 30% peak were pooled and added to 7K MWCO dialysis tubing (ThermoFisher, cat no. 68700) with 3C protease (Genescript, cat no. Z03092) to cleave the N-terminal His tag on NACα. Pooled fractions were dialyzed overnight at 4°C in dialysis buffer (50 mM HEPES-KOH pH 7.5, 150 mM KOAc, 10% glycerol, 6 mM β-mercaptoethanol). Dialyzed proteins were loaded

ARTICLE IN PRESS

onto a HiTrap Q HP column (Cytiva, cat no. 17115401) using a P1 pump and the column was washed with 1-2 CV of ion exchange buffer A (50 mM HEPES-KOH pH 7.5, 2 mM DTT, 2 mM EDTA, 10% glycerol). The column was moved to the Akta and bound proteins were eluted from the column using a linear gradient of ion exchange buffer B to 50% (50 mM HEPES-KOH pH 7.5, 1 M NaCl, 2 mM DTT, 2 mM EDTA, 10% glycerol). Fractions eluted with ~30% ion exchange buffer B were combined and concentrated using an Amicon Ultra 4 mL centrifugal filter (Millipore, cat no. UFC801024). One volume of ion exchange buffer A was added to the sample and the concentration of NAC was determined on the Nanodrop (ThermoFisher) using a molar extinction coefficient, 2980 M^{-1} cm^{-1}. The samples were snap frozen in liquid nitrogen and stored at -80 °C. Purified NAC was resolved by SDS-PAGE and gels were stained with Coomassie R-250 (Sigma, cat no. B-0149).

NAC labeling

WT NACα/NACβ(S57C) and ribosome-binding mutants were labeled with maleimide-Cy3B (Cytiva). The protein was exchanged into Labeling buffer (50 mM KHEPES, pH 7.5, 100 mM NaCl, 1 mM TCEP, 20% glycerol) and incubated with a 5-fold molar excess of dye for 2 hours at room temperature. Free dye was removed using a G-25 Sephadex size exclusion column (GE Healthcare). Fractions containing labeled NAC were identified by SDS-PAGE, pooled, and concentrated to 100-250 μM.

Purification and labeling of SRP subunits

Purification of SRP9/14, SRP19, SRP54, and SRP68/72 were described previously[43]. The single cysteine mutants SRP19(K64C) and SRP54(S12C) were purified as for WT proteins and labeled with maleimide-Atto550 and maleimide-Atto647N (ATTO-TEC), respectively, following

ARTICLE IN PRESS

published protocols[16,43]. Briefly, SRP19(K64C) and SRP54(S12C) were incubated with 2 mM DTT for 30 minutes at 25 °C. Reduced proteins were exchanged into the Labeling buffer by passing twice through a micro Bio-Spin column packed with Bio-Gel P-6 resin (Bio-Rad). Proteins were incubated with an 8-fold molar excess of maleimide dye for 3 hours at 4°C. The labeling reaction was quenched with 2 mM DTT, and excess dye was removed using the G-25 Sephadex Fine size exclusion column (GE Healthcare) run in the labeling buffer (50 mM KHEPES, pH 7.5, 300 mM NaCl, 2 mM EDTA, 1 mM TCEP, 10% Glycerol). Fractions containing labeled SRP subunits were identified by SDS-PAGE, pooled, and concentrated to ~40 µM.

ARTICLE IN PRESS

SRP assembly

SRP was assembled following the protocol established by Lee *et al*[43]. Purified and folded 7SL SRP RNA was incubated in the binding buffer (20 mM Tris, pH 7.5, 300 mM KOAc, 5 mM $Mg(OAc)_2$, 5 mM DTT, 10% Glycerol) at 37 °C. Subsequently, the assembly reaction was performed in the HKMN buffer (50 mM KHEPES, pH 7.5, 500 mM KOAc, 5 mM $Mg(OAc)_2$, 1 mM DTT, 0.02% NIKKOL) with the sequential addition of the protein subunits in the following order: SRP19(K64C)-Atto550 for 10 minutes, SRP68/72 together with SRP9/14 for 10 min, and SRP54(S12C)-Atto647N for 30 minutes at 37 °C. Holo-SRP was purified on a DEAE-Sephadex anion exchange column (Sigma). Fractions containing fully assembled SRP were eluted in a buffer containing 600 mM KOAc, identified by A_{260} measurements, pooled, and stored at -80 °C. The activity of purified SRP was tested using a translocation assay with preprolactin as the SRP substrate using salt-washed ER microsomes incubated in wheat germ extracts[16].

PCR and in vitro Transcription

ARTICLE IN PRESS

A construct encoding for the mitochondrial matrix protein HSP60[21], and gblocks (Integrated DNA Technologies) encoding the N-terminus of mitochondrial inner membrane protein $OXA1L_{MTS}$ (AAs 2-51, AMGLMCGRRELLRLLQSGRRVHSVAGPSQWLGKPLTTRLLFPAAPCCCRP) or $OXA1L_{\Delta MTS}$ (deletion of MTS residues LMCGRRELLRLLQSGRRV), was PCR amplified to include the upstream T7 promoter, 3X-FLAG tag, and the N-terminus of each nascent chain. OXA1L constructs used for cryo-EM contained a C-terminal modified XBP1 ribosome stalling peptide (AAs 237-260, DPVPYQPPFLCQWGRHQCAWKPLM). PCR products were then cleaned up using the QIAquick PCR Purification Kit (Qiagen, cat no. 28104). The resulting purified PCR products were *in vitro* transcribed for 4 hours at 38 °C, using 1.1 mg/mL T7 polymerase in reaction buffer (40 mM Tris-HCl pH 7.6, 5 mM ribonucleoside triphosphates, 6 mM $MgCl_2$, 2 mM spermidine, 1 mM DTT, 0.04 U/µL RNase Inhibitor) or with the T7 HiScribe kit (NEB, cat no. E2040S). Following the reaction period, the precipitate was pelleted at ~22,000 x g for 5 minutes at 4°C. The supernatant was transferred to a sterile 1.5 mL tube and 6M LiCl was added 1:1 for 1 hour on ice. After the incubation period, the mixture was centrifuged at ~22,000 x g for 20 minutes at 4°C and the supernatant was discarded. The pellet was washed with 200 µL of ice cold 70% ethanol and centrifuged at ~22,000 x g for 5 minutes at 4°C. The supernatant was discarded and 100 µL of sterile ultrapure water was used to resuspend the pellet. The sample was placed on ice and 40 µL of 2.8 M NaOAc and 300 µL 95% ice cold ethanol were added. The mixture was incubated on ice for 5 minutes and centrifuged at ~22,000 x g for 30 minutes at 4°C. The resulting pellet was washed with 200 µL of 70% ethanol and centrifuged at ~22,000 x g for 5 min at 4°C. The supernatant was discarded, and the resulting purified RNA was resuspended in 100 µL of sterile ultrapure water.

RNC purification for cryo-EM

ARTICLE IN PRESS

ARTICLE IN PRESS

Rabbit reticulocyte lysates (Promega, cat no. L4540) were reacted with HSP60 or OXA1L RNA after diluting the lysate in buffer (final concentration: RNase Inhibitor (Promega) 0.04 U/μL, 0.5X protease inhibitor (Promega), 24 μM amino acid mix, 81 mM KCl, 0.67 mM $Mg(OAc)_2$). The reaction was incubated at 32 °C for 25 minutes and then placed on ice.

A 1 mL polypropylene gravity column (Qiagen, cat no. 34924) was loaded with Anti-DYKDDDK G1 affinity resin (GenScript, cat no. L00432 or Sigma, cat no. A2220). The column was rinsed with 10 bead volumes of 1X PBS followed by 10 bead volumes of low-salt wash buffer (50 mM HEPES-KOH pH 7.7, 100 mM KCl, 10 mM $MgCl_2$). The RRL reaction was added to the column and incubated for 2 hours at 4°C with rotation. After the incubation period, the cap and side walls of the gravity column were rinsed with high-salt wash buffer (50 mM HEPES-KOH pH 7.7, 750 mM KOAc, 10 mM $Mg(OAc)_2$, 0.1% Triton-X, 1 mM DTT). The reaction supernatant was run through the column and the beads were subsequently washed with 10 bead volumes of high-salt wash buffer (2X) followed by 10 bead volumes of low-salt wash buffer (2X). RNCs were incubated with elution buffer (50 mM HEPES-KOH pH 7.7, 100 mM KOAc, 15 mM $Mg(OAc)_2$) containing 0.25 mg/mL FLAG peptide for 15 minutes at RT (5X). The eluted fractions were placed on ice and combined to a total volume of 500 μL and centrifuged at 100,000 rpm for 1 hr at 4°C using the TLA120.1 rotor (Beckman). The pellet was resuspended in base elution buffer by gently pipetting up and down. The ribosome concentrations were determined using RNA reading at A260 on the Nanodrop. RNCs were snap frozen in liquid nitrogen and stored at -80 °C.

RNC labelling and purification for smTIRFM

In vitro translations used a pUC19 vector containing, from 5' to 3', a T7 promoter, encephalomyocarditis virus (EMCV) internal ribosome entry site (IRES), 3xFLAG-tag, and 3C

ARTICLE IN PRESS

ARTICLE IN PRESS

protease site. DNA fragment encoding the nascent chain of preprolactin or OXA1L was cloned after the 3C protease site using Gibson assembly. In the $OXA1L_{\Delta MTS}$ construct, an amphipathic helical region (MTS) of the OXA1L presequence (LMCGRRELLRLLQSGRRV, residues 4-21) was deleted, whereas in the $OXA1L_{MTS\text{-}to\text{-}SS}$ the deleted region was swapped with signal sequence of preprolactin (LLLLLLVSNLLL, residues 13-24). For fluorescent labeling of the RNCs, an amber codon was introduced at residue 39 in the OXA1L nascent chain using QuickChange mutagenesis.

PCR fragments encoding the region from the T7 promoter to Ser74 of OXA1L or Phe80 of preprolactin were transcribed using the T7 MegaScript protocol in the presence of 5 mM 5'-biotin-G-monophosphate (TriLink). The resulting mRNAs were translated in rabbit reticulocyte lysate (RRL, Green Hectares) supplemented with 1 µM *Methanosarcina mazei* pyrrolysine synthase (*Mm*PylRS), 10 mg/L *M. mazei* amber suppressor tRNA (*Mm*PyltRNA), and 100 µM axial trans-cyclooct-4-en-L-lysine (TCOK, SiChem), for 30 minutes at 32 °C[16].

The translation reaction was layered on a High Salt Sucrose Cushion (50 mM KHEPES, pH 7.5, 1 M KOAc, 15 mM $Mg(OAc)_2$, 0.5 M Sucrose, 0.1% Triton, 2 mM DTT) at a volumetric ratio of 2:3. The ribosomal fraction was pelleted by ultracentrifugation (100k rpm for 45 minutes at 4°C) in a TLA100.3 rotor (Beckman Coulter). Pellets were resuspended in RNC buffer (50 mM KHEPES, pH 7.5, 150 mM KOAc, 2 mM $Mg(OAc)_2$) to 1 µM ribosome concentration and incubated with 1 µM tetrazine-conjugated Atto647N dye (Jena Biosciences) for 30 minutes at 25 °C, to allow for the Diels-Alder cycloaddition reaction. Labeled RNCs were incubated with anti-DYKDDDK magnetic agarose (Pierce) pre-equilibrated in RNC buffer for 1 hour at 4°C with constant rotation. Beads were washed sequentially with 10 bead volumes of RNC buffer containing

ARTICLE IN PRESS

ARTICLE IN PRESS

300 mM KOAc, RNC buffer containing 0.1% Triton, and RNC buffer. RNC was eluted with 1.5 mg/ml 3xFLAG (DYKDDDK) peptide for 30 minutes at 4°C with constant rotation. The eluted RNCs were incubated with 1 μM 3C protease (GoldBio) for at least 2 hours at 25°C, and sedimented using a High Salt Sucrose Cushion at a volumetric ratio of 2:3 at 100k rpm for 30 minutes at 4°C in a TLA120.2 rotor (Beckman Coulter). Pelleted RNC was resuspended in storage buffer (50 mM KHEPES, pH 7.5, 150 mM KOAc, 5 mM $Mg(OAc)_2$, 0.04% NIKKOL, 2 mM DTT) to ~100 nM (ribosome concentration). The presence of fluorescently labeled nascent chain was confirmed by SDS-PAGE and fluorescence scanning for Atto647N signal (Typhoon biomolecular imager, Cytiva). Fluorescently labeled RNCs were snap frozen in liquid nitrogen and stored at -80 °C.

Single-molecule TIRF microscopy

Surfaces of pure quartz imaging slides and coverslips were aminosilanized with vectabond (Vector lab) and coated with biotin-PEG (Laysan Bio). Slides were passivated with passivation buffer (1X Tween-20, 1 mg/ml BSA) for at least 1 hour at 25 °C, washed with 50 mM KHEPES, pH 7.5, and incubated with 0.5 mg/ml NeutrAvidin (ThermoFisher) for 10 minutes. Unbound NeutrAvidin was washed away with Imaging Buffer, which constitutes Assay Buffer (50 mM KHEPES, pH 7.5, 150 mM KOAc, 5 mM $Mg(OAc)_2$, 0.04% NIKKOL, 2 mM DTT) supplemented with 1 mg/ml BSA, 4 mM Trolox, 2.5 mM protocatechuic acid (PCA), and 50 nM protocatechuate-3,4-dioxygenase from *Pseudomonas sp.* (PCD, Sigma)[48]. For assays involving SRP, the imaging buffer further included 200 μM non-hydrolyzable GTP analog, guanosine-5′-[(β,γ)-imido]triphosphate (GppNHp).

ARTICLE IN PRESS

ARTICLE IN PRESS

RNC with 3'-biotinylated mRNA was diluted to 1.5 nM in Imaging Buffer and immobilized on NeutrAvidin-coupled slides for 10 minutes at 25 °C. For experiments with NAC, RNC-coated slides were then flushed with 2 nM WT or mutant Cy3B-labeled NAC in Imaging Buffer. For experiments involving NAC and SRP, 1.5 nM doubly labeled SRP and 2 nM unlabeled WT or mutant NAC were incubated in Imaging Buffer for 5 minutes and loaded onto slides with immobilized RNCs.

Movies were recorded using MicroManager on a custom-built TIRF microscopy setup[49]. The presence of immobilized Atto647N-conjugated RNCs was confirmed by excitation at 635 nm. Movies were recorded by excitation at 532 nm (donor dye; Atto550 or Cy3B) in single-excitation mode and detection of both the donor and acceptor channels, with a temporal resolution of 50 ms.

Analysis of smTIRF microscopy data

Donor and acceptor channel image series were aligned and analyzed using iSMS software[50]. FRET efficiencies were calculated based on the raw intensity of donor and acceptor fluorescence time traces and were corrected for background noise and γ factor, which accounts for the difference in quantum yield between the dyes and leakage of donor fluorescence to the acceptor channel. Apparent FRET efficiency (E_{app}) was calculated using Equation 1,

$$E_{\mathrm{app}} = \frac{I_{\mathrm{DD}}}{I_{\mathrm{DD}} + I_{\mathrm{AD}}} \quad (1)$$

in which I_{DD} and I_{AD} are the fluorescence intensities of the donor and acceptor dye, respectively, upon excitation of the donor. FRET traces from all movies of the same sample were combined and analyzed using Hidden Markov Modeling (HMM) available in the iSMS software. The number of FRET states was established by applying Bayesian information criterion. These analyses yielded

ARTICLE IN PRESS

three FRET populations and the mean FRET efficiency for each state. These parameters were used for Gaussian fitting of the FRET histograms according to Eq 2,

$$\mathrm{PDF} = \sum_{i=1}^{n} A_i \cdot \frac{1}{\sigma_i\sqrt{2\pi}} e^{-\frac{1}{2}\left(\frac{E-\mu_i}{\sigma_i}\right)^2} \quad (2)$$

in which PDF is the probability density function, n is the number of FRET states detected and is set to 3 (determined by HMM), A_i is the weight of the ith Gaussian, and σ_i and μ_i are the standard deviation and center (determined by HMM) of the ith Gaussian.

To determine the residence time of NAC on RNC, cumulative fluorescence intensity signal ($I_{\mathrm{cumulative}}$) was calculated using Eq 3,

$$I_{\mathrm{cumulative}} = I_{\mathrm{AD}} + \gamma \cdot I_{\mathrm{DD}} \quad (3)$$

and plotted over time for each trace. Colocalization of labeled NAC and RNC identified by $I_{\mathrm{cumulative}}$ over background noise. Two-state HMM was then used to distinguish bound versus dissociated NAC and determine the dwell time of each colocalization event (t). The cumulative probability distribution of t was fitted to Eq 4,

$$f(t) = A_{\mathrm{fast}} \cdot e^{-k_{\mathrm{fast}} \cdot t} + A_{\mathrm{slow}} \cdot e^{-k_{\mathrm{slow}} \cdot t} \quad (4)$$

in which A_{fast} and A_{slow} are the amplitudes of the fast and slow-dissociating populations, and k_{fast} and k_{slow} are the respective dissociation rate constants.

Cryo-EM sample preparation and data acquisition

FLAG-SUMO-HSP60 RNCs (~350 ng/uL) were reacted with 260 nM SUMO protease (Trialtus, cat no 30-1030) at 30°C for 20 minutes. NAC was added at a final concentration of 2 μM in

reaction buffer (50 mM HEPES-KOH pH 7.7, 100 mM KOAc, 15 mM $Mg(OAc)_2$, 0.01875% GDN) for 20 minutes at 30°C. The reaction was moved to ice prior to freezing grids. Quantifoil R2/1 300 mesh copper grids (Quantifoil, cat no. Q350CR1) were freshly coated with 3.3 nm carbon and glow discharged at 15 mA for 15 seconds using an EMS glow discharger. A 5 µL drop of the NAC-RNC reaction was incubated for 1 minute on the grid at 100% relative humidity and 4°C before blotting. The grid was subsequently plunge frozen into a cup filled with liquid ethane pre-cooled to liquid nitrogen temperatures. Cryo-EM data was collected on the ThermoFisher Glacios electron microscope operated at 200 kV and equipped with a Falcon4 direct electron detector at a total magnification of 120,000x using a defocus range of -2.2 to -1.2 and a step size of 0.2. Movies were collected at a pixel size of 1.2 Å with a dose of 50 e/Å^2 across 40 frames per movie.

ARTICLE IN PRESS

FLAG-3C-OXA1L$_{MTS}$ and FLAG-3C-OXA1L$_{\Delta MTS}$ RNCs (~200-250 ng/uL) were reacted with 250 nM 3C protease at 30°C for 20 minutes. NAC was added at a final concentration of 1 µM in reaction buffer (50 mM HEPES-KOH pH 7.7, 100 mM KOAc, 15 mM $Mg(OAc)_2$, 0.02% C12E8) for 20 minutes at 30°C. The reaction was moved to ice prior to freezing grids. Quantifoil R2/1 300 mesh copper grids (Quantifoil, cat no. Q350CR1) were freshly coated with 3.3 nm carbon and glow discharged at 15 mA for 15 seconds using an EMS glow discharger. A 5 µL drop of the NAC-RNC reaction was incubated for 1 minute on the grid at 100% relative humidity and 4°C before blotting. The grid was subsequently plunge frozen into a cup filled with liquid ethane pre-cooled to liquid nitrogen temperatures. Cryo-EM data was collected on the ThermoFisher Krios electron microscope operated at 300 kV and equipped with a K3 direct electron detector at a total magnification of 105,000x with an energy filter slit width of 10 eV, using a defocus range of -1.4 to -0.8 with a step size of 0.2. Movies were collected at a pixel size of 0.83 Å with a dose of 32 e/Å^2 (OXA1L$_{MTS}$) or 40 e/Å^2 (OXA1L$_{\Delta MTS}$) across 40 frames per movie.

ARTICLE IN PRESS

Cryo-EM data processing strategy for HSP60 RNC_{MTS}

Movies were motion-corrected, dose-weighted, and the contrast transfer function (CTF) was estimated in CryoSPARC[51,52]. Template picker was used to pick particles with a diameter of 250 Å from the resulting micrographs. A total of 1,366,067 particles were extracted from 8,780 micrographs at a box size of 512 x 512 pixels. The extracted particles underwent 2D classification, with ribosome classes selected for further processing. A homogenous refinement of the selected 519,343 particles yielded a consensus 80S ribosome map at 2.97 Å. Following refinement, translating ribosomes with P-site tRNA density were classified using a spherical mask on the A/P/E by conducting a 3D variability analysis in CryoSPARC[53]. Particles with a stable P-site tRNA density were refined separately and subjected to an additional 3D variability analysis, using a spherical mask on the exit tunnel to identify particles with strong NAC density. An additional 3D variability analysis was conducted on the exit tunnel to remove particles with noisy artifacts. The final set of 36,986 particles with stable NAC and P-site tRNA density were polished using the reference-based motion correction package implemented in CryoSPARC. A homogenous refinement was conducted on the polished particles which yielded the HSP60 NAC-RNC_{MTS} map at a global resolution of 3.04 Å- determined by the gold standard Fourier Shell Correlation (FSC) of two half-sets of particles processed independently with an FSC threshold of 0.143. The local resolution of the map was calculated in CryoSPARC at an FSC threshold of 0.143.

Cryo-EM data processing strategy for OXA1L RNC_{MTS} and OXA1L $RNC_{\Delta MTS}$

Both OXA1L RNC_{MTS} and OXA1L $RNC_{\Delta MTS}$ were processed in the same manner. Movies were motion and CTF corrected in CryoSPARC. Blob picker was used to pick particles with a diameter of 250-400 Å. Picked particles were extracted at a box size of 512 x 512 pixels and binned to 128

x 128 pixels for 2D classification. Ab-initio reconstruction was used to generate reference maps for 3D classification of all extracted particles to select 80S ribosome particles and exclude poorly aligning or junk particles. A homogenous refinement was conducted on the final set of 80S ribosome particles. Subsequent 3D variability analyses were conducted to sort for particles with stable P-site tRNA and NAC density using focused spherical masks. Particles were re-extracted at full pixel size and refined yielding high-resolution maps of ribosomes translating the OXA1L MTS and the MTS deletion mutant of OXA1L. The local resolution was calculated in CryoSPARC at an FSC threshold of 0.143.

Model Building

Following data processing, a model of the 80S ribosome (PDB 6R5Q) and NAC (PDB 7QWR) was docked into the cryo-EM map using ChimeraX[54]. NAC and eL22 were further fitted into the map as rigid bodies in Coot and manually adjusted based on side chain densities observed in the map. The unresolved N-terminal fluke of NACβ was built *de novo* guided by the visible side chain density. PHENIX[55] was used to refine the model in the NAC-RNC$_{MTS}$ density map with 3 macrocycles of real space refinements applying Ramachandran, sidechain rotamer, and protein secondary structure to correct for clashes. The final model was validated using MolProbity in PHENIX and figures were made in ChimeraX.

Isolation of Ribosomes from HEK293 Cells

Ribosomes were isolated from HEK293 GnTI cell pellets. Cell pellets were resuspended in lysis buffer (50 mM HEPES-KOH pH 7.7, 100 mM KOAc, 5 mM $Mg(OAc)_2$, 0.5% IGEPAL, 1 mM DTT, 0.5X Protease inhibitor (Promega), 0.04 U/µL RNase inhibitor (Promega)) and lysed by passing the resuspension through a 23G x 1 ¼ needle four times (BD, cat no. 305120). The lysate

ARTICLE IN PRESS

was centrifuged at 11,000 x g for 10 min at 4°C. The supernatant was layered 1:1 on a sucrose cushion (50 mM HEPES-KOH pH 7.7, 750 mM KOAc, 5 mM $Mg(OAc)_2$, 2 mM TCEP, 30% sucrose (w/v)) and centrifuged at 100,000 rpm for 1 hr at 4°C using a TLA 120.1 rotor. The pellets were resuspended in ribosome buffer (50 mM HEPES-KOH pH 7.7, 100 mM KOAc, 2 mM $Mg(OAc)_2$, 2 mM TCEP, 0.5X protease inhibitor, 0.04 U/µL RNase inhibitor (Promega)). The concentration was determined on the Nanodrop (ThermoFisher) and aliquots of isolated ribosomes were snap frozen in liquid nitrogen.

NAC-Ribosome Co-sedimentation Assay

NAC variants and ribosomes were thawed on ice. Ribosomes were centrifuged at ~19,000 x g for 10 min at 4°C and the supernatant was transferred to a sterile 1.5 mL tube. NAC was diluted to 10 µM in reaction buffer (50 mM HEPES-KOH pH 7.7, 100 mM KOAc, 15 mM $Mg(OAc)_2$, 0.04 U/µL RNase Inhibitor (Promega)). Ribosomes were diluted to 13 A260 units/mL in reaction buffer and NAC variants were added at a final concentration of 0.2 µM. The reaction was incubated at 30°C for 20 minutes and then moved to ice. A 50 µL portion of the reaction was layered on top of a sucrose cushion (50 mM HEPES-KOH pH 7.7, 100 mM KOAc, 15 mM $Mg(OAc)_2$, 0.5X protease inhibitor (Promega), 0.04 U/µL RNase inhibitor (Promega), 25% sucrose (w/v)) and centrifuged at 100,000 rpm for 1 hr at 4°C using a TLA 120.1 rotor (Beckman). The pellet was resuspended in 1X SDS-PAGE loading dye (50 mM Tris-HCl pH 6.8, 2% SDS, 1% β-mercaptoethanol, 6% glycerol, 0.004% bromophenol blue) for analysis by Western Blot.

ARTICLE IN PRESS

CRISPR/Cas9-based Knockout HEK293T cells

HEK293T cells, obtained from ATCC, were cultured at 37°C with 5% CO2 in DMEM with 10% fetal bovine serum (Fisher Scientific). Generation of *NACβ*-KO HEK293T cells was performed

ARTICLE IN PRESS

using CRISPR/Cas9. sgRNA oligonucleotide designed for human NACβ (5'-TGCTCGCAGAAAGAAGAAGG-3') was inserted into lentiCRISPR, version 2 (Addgene 52961). Cells grown in 10 cm petri dishes were transfected with indicated plasmids using 5 µl 1 mg/ml polyethylenimine (PEI) (Millipore Sigma) per 1 µg of plasmids for HEK293T cells. The cells were cultured 24 hours after transfection in medium containing 2 µg/ml puromycin for 24 hours and then in normal growth medium. Single cell isolations were conducted to select for HEK293T cells with NACβ knocked out.

Thapsigargin (TG) treatment

HEK293T cells treated with 100 nM thapsigargin for 4 hours were included as positive controls for ER stress.

RNA preparation and Reverse Transcription PCR (RT-PCR)

XBP1 splicing was assessed in HEK293T cells as described previously[56,57]. Briefly, total RNA was extracted from cells using TRI Reagent and BCP phase separation reagent (Molecular Research Center, TR 118). RT-PCR primer sequences are:

hXBP1: F: 5'-GAATGAAGTGAGGCCAGTGG-3' R: ACTGGGTCCTTCTGGGTAGA- 3'

hL32 F: 5'-AGTTCCTGGTCCACAACGTC-3' R: 5'-TTGGGGTTGGTGACTCTGAT- 3'

h- denotes human genes.

Plasmids

Gene sequences encoding NACα and NACβ were synthesized and cloned into a pcDNA3.1(+)C-(K)-DYK vector (Genscript). QuickChange site-directed mutagenesis (Agilent, cat. no. 210518) was used to introduce two stop codons upstream of the C-terminal FLAG tag in NACβ, and to

ARTICLE IN PRESS

ARTICLE IN PRESS

generate NAC switch mutants in which His34 and Arg35 or Lys42 and Phe46 were mutated to alanine (termed HR:AA and KF:AA, respectively).

NAC Rescue Experiments

NACβ-KO HEK293T cells grown in 3.5 or 10 cm petri dishes were transfected with 1 μg indicated plasmids with 5 μl 1mg/ml Polyethylenimine Max (PEI MAX) (Polysciences, 24765). Where indicated, cells were co-transfected with plasmids to express NACα and NACβ, or an empty vector. The cells were cultured for 24 hours after transfection, then pelleted and snap-frozen in liquid nitrogen for Western Blot or pulldown experiments. The proteins were extracted by sonication in NP-40 lysis buffer (50 mM Tris-HCl at pH7.5, 150 mM NaCl, 1% NP-40, 1 mM EDTA) with protease inhibitor (Millipore Sigma), DTT (Millipore Sigma, 1 mM), and phosphatase inhibitor cocktail (Millipore Sigma). Lysates were incubated on ice for 30 minutes and centrifuged at 16,000 x g for 10 minutes. Supernatants were collected and analyzed for protein concentration using Bio-Rad Protein Assay Dye (Bio-Rad). From 10 to 30 μg of protein was denatured at 95°C for 5 minutes in 5× SDS sample buffer (250 mM Tris-HCl pH 6.8, 10% sodium dodecyl sulfate, 0.05% bromophenol blue, 50% glycerol, and 1.44 M β-mercaptoethanol).

ARTICLE IN PRESS

Glycoprotein Isolation by ConA Affinity Pulldown

ConA pulldown was performed using the Thermo Scientific Glycoprotein Isolation Kit (ThermoFisher, cat no. 89804) according to the manufacturer's instructions with minor modifications. Briefly, the kit's Binding/Wash Buffer was supplemented with 1% NP-40 and used as the lysis buffer. Frozen cell pellets were lysed in this buffer at 4°C in the presence of protease and phosphatase inhibitors. Lysates were centrifuged, and the supernatant was collected and diluted fourfold to reduce the NP-40 concentration. Approximately 3 mg of total protein was

ARTICLE IN PRESS

incubated with 50 µL ConA resin overnight at 4°C with gentle rocking. The resin was then washed four times with Binding/Wash Buffer, and bound glycoproteins were eluted with 100 µL Elution Buffer. Eluates were mixed with SDS sample buffer and analyzed by SDS-PAGE followed by immunoblotting.

Western Blot

Proteins were resolved by SDS–PAGE using either Bis-Tris gels (GenScript, cat. nos. M00653, M00654; Thermo Fisher, cat. no. NP0323BOX) run in MES buffer (GenScript, cat. no. M00677) or Tris-glycine gels, and then transferred to either 0.2 µm nitrocellulose membranes (LI-COR, cat. no. 926-31092) or PVDF membranes (Thermo Fisher). Membranes were blocked in 5% (w/v) milk in 1x PBST (0.1% Tween-20) for 1 h at room temperature, then incubated with primary antibodies diluted in 2% (w/v) BSA in 1x PBST. Primary antibodies used were: anti-FLAG (Sigma, F1804, 1:1,000), anti-RPL10a (Invitrogen, MA5-44710, 1:2,000), anti-HSP90 (Santa Cruz, sc-13119, 1:5,000), anti-BiP (Abcam, ab21685, 1:5,000), anti-PDI (Enzo, ADI-SPA-890, 1:5,000), anti-NACα (Biorbyt, orb411671, 1:1,000), anti-NACβ (Invitrogen, PA5-63299, 1:2,000), and anti-CARL (Proteintech, 27298-1-AP, 1:5,000). Fluorescent secondary antibodies (anti-mouse, Invitrogen A21058; anti-rabbit, Invitrogen A32735, 1:10000) were detected using a LI-COR Odyssey imager. For chemiluminescent detection, HRP-conjugated secondary antibodies (Bio-Rad, 1:10,000) were incubated for 1 h at room temperature and developed using the ECL Chemiluminescence Detection System (Bio-Rad). Band intensities were quantified using Image Lab software (Bio-Rad, v6.1). Uncropped blots and gels are supplied in the source data file.

ARTICLE IN PRESS

Data Availability

ARTICLE IN PRESS

The cryo-EM maps and corresponding atomic models generated in this study have been deposited in the PDB and EMDB under accession code: EMD-48552 [https://www.ebi.ac.uk/emdb/EMD-48552] and PDB-9MR4 [https://doi.org/10.2210/pdb9mr4/pdb] for the OXA1L NAC-RNC$_{MTS}$ structure; EMD-71310 [https://www.ebi.ac.uk/emdb/EMD-71310] for HSP60 NAC-RNC$_{MTS}$; EMD-71286 [https://www.ebi.ac.uk/emdb/EMD-71286] and EMD-71287 [https://www.ebi.ac.uk/emdb/EMD-71287] for the H59-undocked and -docked barrel states of the OXA1L$_{\Delta MTS}$ structure, respectively. All data related to this study are available in the main text or the supplementary material. Source data are provided with this paper.

ARTICLE IN PRESS

References

1. Morales-Polanco, F., Lee, J. H., Barbosa, N. M. & Frydman, J. Cotranslational Mechanisms of Protein Biogenesis and Complex Assembly in Eukaryotes. *Annu. Rev. Biomed. Data Sci.* **5**, 67–94 (2022).
2. Hegde, R. S. & Keenan, R. J. The mechanisms of integral membrane protein biogenesis. *Nat. Rev. Mol. Cell Biol.* **23**, 107–124 (2022).
3. Gamerdinger, M. & Deuerling, E. Cotranslational sorting and processing of newly synthesized proteins in eukaryotes. *Trends Biochem. Sci.* **49**, 105–118 (2024).
4. Rabl, L. & Deuerling, E. The nascent polypeptide-associated complex (NAC) as regulatory hub on ribosomes. *Biol. Chem.* **406**, 295–307 (2025).
5. Truscott, K. N., Brandner, K. & Pfanner, N. Mechanisms of Protein Import into Mitochondria. *Curr. Biol.* **13**, R326–R337 (2003).
6. Dudek, J., Rehling, P. & van der Laan, M. Mitochondrial protein import: Common principles and physiological networks. *Biochim. Biophys. Acta BBA - Mol. Cell Res.* **1833**, 274–285 (2013).

7. Wiedemann, N. & Pfanner, N. Mitochondrial Machineries for Protein Import and Assembly. *Annu. Rev. Biochem.* **86**, 685–714 (2017).
8. Gamerdinger, M., Hanebuth, M. A., Frickey, T. & Deuerling, E. The principle of antagonism ensures protein targeting specificity at the endoplasmic reticulum. *Science* **348**, 201–207 (2015).
9. Deng, J. M. & Behringer, R. R. An insertional mutation in theBTF3 transcription factor gene leads to an early postimplantation lethality in mice. *Transgenic Res.* **4**, 264–269 (1995).
10. Markesich, D. C., Gajewski, K. M., Nazimiec, M. E. & Beckingham, K. bicaudal encodes the *Drosophila* beta NAC homolog, a component of the ribosomal translational machinery. *Development* **127**, 559–572 (2000).
11. Bloss, T. A., Witze, E. S. & Rothman, J. H. Suppression of CED-3-independent apoptosis by mitochondrial βNAC in Caenorhabditis elegans. *Nature* **424**, 1066–1071 (2003).
12. Raue, U., Oellerer, S. & Rospert, S. Association of Protein Biogenesis Factors at the Yeast Ribosomal Tunnel Exit Is Affected by the Translational Status and Nascent Polypeptide Sequence. *J. Biol. Chem.* **282**, 7809–7816 (2007).
13. Wiedmann, B., Sakai, H., Davis, T. A. & Wiedmann, M. A protein complex required for signal-sequence-specific sorting and translocation. *Nature* **370**, 434–440 (1994).
14. Liu, Y., Hu, Y., Li, X., Niu, L. & Teng, M. The Crystal Structure of the Human Nascent Polypeptide-Associated Complex Domain Reveals a Nucleic Acid-Binding Region on the NACA Subunit. *Biochemistry* **49**, 2890–2896 (2010).
15. Wang, L. *et al.* Crystal structures of NAC domains of human nascent polypeptide-associated complex (NAC) and its αNAC subunit. *Protein Cell* **1**, 406–416 (2010).

ARTICLE IN PRESS

ARTICLE IN PRESS

16. Hsieh, H.-H., Lee, J. H., Chandrasekar, S. & Shan, S. A ribosome-associated chaperone enables substrate triage in a cotranslational protein targeting complex. *Nat. Commun.* **11**, 5840 (2020).

17. Wegrzyn, R. D. *et al.* A Conserved Motif Is Prerequisite for the Interaction of NAC with Ribosomal Protein L23 and Nascent Chains. *J. Biol. Chem.* **281**, 2847–2857 (2006).

18. Pech, M., Spreter, T., Beckmann, R. & Beatrix, B. Dual Binding Mode of the Nascent Polypeptide-associated Complex Reveals a Novel Universal Adapter Site on the Ribosome. *J. Biol. Chem.* **285**, 19679–19687 (2010).

19. Jomaa, A. *et al.* Mechanism of signal sequence handover from NAC to SRP on ribosomes during ER-protein targeting. *Science* **375**, 839–844 (2022).

20. Alamo, M. D. *et al.* Defining the Specificity of Cotranslationally Acting Chaperones by Systematic Analysis of mRNAs Associated with Ribosome-Nascent Chain Complexes. *PLoS Biol.* **9**, e1001100 (2011).

21. Gamerdinger, M. *et al.* Early Scanning of Nascent Polypeptides inside the Ribosomal Tunnel by NAC. *Mol. Cell* **75**, 996-1006.e8 (2019).

22. Lentzsch, A. M. *et al.* NAC guides a ribosomal multienzyme complex for nascent protein processing. *Nature* **633**, 718–724 (2024).

23. Gamerdinger, M. *et al.* NAC controls cotranslational N-terminal methionine excision in eukaryotes. *Science* **380**, 1238–1243 (2023).

24. Klein, M., Wild, K. & Sinning, I. Multi-protein assemblies orchestrate co-translational enzymatic processing on the human ribosome. *Nat. Commun.* **15**, 7681 (2024).

25. Gamerdinger, M. *et al.* Mechanism of cotranslational protein N-myristoylation in human cells. *Mol. Cell* **85**, 2749-2758.e8 (2025).

ARTICLE IN PRESS

26. Zdancewicz, S., Maldosevic, E., Malezyna, K. & Jomaa, A. NAC couples protein synthesis with nascent polypeptide myristoylation on the ribosome. *EMBO J.* **44**, 6320–6342 (2025).
27. Denk, T. *et al.* Structural basis of co-translational N-myristoylation in humans. *Nat. Commun.* **17**, 1191 (2026).
28. Yudin, D. *et al.* Mechanism of cotranslational modification of histones H2A and H4 by MetAP1 and NatD. *Sci. Adv.* **11**, eaeb1017 (2025).
29. Zhang, Y. *et al.* NAC functions as a modulator of SRP during the early steps of protein targeting to the endoplasmic reticulum. *Mol. Biol. Cell* **23**, 3027–3040 (2012).
30. Nyathi, Y. & Pool, M. R. Analysis of the interplay of protein biogenesis factors at the ribosome exit site reveals new role for NAC. *J. Cell Biol.* **210**, 287–301 (2015).
31. Powers, T. & Walter, P. The nascent polypeptide-associated complex modulates interactions between the signal recognition particle and the ribosome. *Curr. Biol.* **6**, 331–338 (1996).
32. Jomaa, A. *et al.* Molecular mechanism of cargo recognition and handover by the mammalian signal recognition particle. *Cell Rep.* **36**, 109350 (2021).
33. Kobayashi, K. *et al.* Structure of a prehandover mammalian ribosomal SRP·SRP receptor targeting complex. *Science* **360**, 323–327 (2018).
34. Lee, J. H. *et al.* Receptor compaction and GTPase rearrangement drive SRP-mediated cotranslational protein translocation into the ER. *Sci. Adv.* **7**, eabg0942 (2021).
35. Costa, E. A., Subramanian, K., Nunnari, J. & Weissman, J. S. Defining the physiological role of SRP in protein-targeting efficiency and specificity. *Science* **359**, 689–692 (2018).
36. Vögtle, F.-N. *et al.* Global Analysis of the Mitochondrial N-Proteome Identifies a Processing Peptidase Critical for Protein Stability. *Cell* **139**, 428–439 (2009).
37. Calvo, S. E. *et al.* Comparative Analysis of Mitochondrial N-Termini from Mouse, Human, and Yeast. *Mol. Cell. Proteomics* **16**, 512–523 (2017).

ARTICLE IN PRESS

ARTICLE IN PRESS

38. von Heijne, G. Mitochondrial targeting sequences may form amphiphilic helices. *EMBO J.* **5**, 1335–1342 (1986).

39. Roise, D., Horvath, S. J., Tomich, J. M., Richards, J. H. & Schatz, G. A chemically synthesized pre-sequence of an imported mitochondrial protein can form an amphiphilic helix and perturb natural and artificial phospholipid bilayers. *EMBO J.* **5**, 1327–1334 (1986).

40. Abe, Y. *et al.* Structural Basis of Presequence Recognition by the Mitochondrial Protein Import Receptor Tom20. *Cell* **100**, 551–560 (2000).

41. Shanmuganathan, V. *et al.* Structural and mutational analysis of the ribosome-arresting human XBP1u. *eLife* **8**, e46267 (2019).

42. Feng, Q. & Shao, S. In vitro reconstitution of translational arrest pathways. *Methods* **137**, 20–36 (2018).

43. Lee, J. H. *et al.* Sequential activation of human signal recognition particle by the ribosome and signal sequence drives efficient protein targeting. *Proc. Natl. Acad. Sci.* **115**, E5487–E5496 (2018).

44. Yoshida, H., Matsui, T., Yamamoto, A., Okada, T. & Mori, K. XBP1 mRNA Is Induced by ATF6 and Spliced by IRE1 in Response to ER Stress to Produce a Highly Active Transcription Factor. *Cell* **107**, 881–891 (2001).

45. Qi, L., Yang, L. & Chen, H. Chapter Eight - Detecting and Quantitating Physiological Endoplasmic Reticulum Stress. in *Methods in Enzymology* (ed. Conn, P. M.) vol. 490 137–146 (Academic Press, 2011).

46. Klein, M. A., Wild, K., Kišonaitė, M. & Sinning, I. Methionine aminopeptidase 2 and its autoproteolysis product have different binding sites on the ribosome. *Nat. Commun.* **15**, 716 (2024).

ARTICLE IN PRESS

ARTICLE IN PRESS

47. Wild, K. *et al.* MetAP-like Ebp1 occupies the human ribosomal tunnel exit and recruits flexible rRNA expansion segments. *Nat. Commun.* **11**, 776 (2020).

48. Aitken, C. E., Marshall, R. A. & Puglisi, J. D. An Oxygen Scavenging System for Improvement of Dye Stability in Single-Molecule Fluorescence Experiments. *Biophys. J.* **94**, 1826–1835 (2008).

49. Shen, K., Arslan, S., Akopian, D., Ha, T. & Shan, S. Activated GTPase movement on an RNA scaffold drives co-translational protein targeting. *Nature* **492**, 271–275 (2012).

50. Preus, S., Noer, S. L., Hildebrandt, L. L., Gudnason, D. & Birkedal, V. iSMS: single-molecule FRET microscopy software. *Nat. Methods* **12**, 593–594 (2015).

51. Zheng, S. Q. *et al.* MotionCor2: anisotropic correction of beam-induced motion for improved cryo-electron microscopy. *Nat. Methods* **14**, 331–332 (2017).

52. Rohou, A. & Grigorieff, N. CTFFIND4: Fast and accurate defocus estimation from electron micrographs. *J. Struct. Biol.* **192**, 216–221 (2015).

53. Punjani, A. & Fleet, D. J. 3D variability analysis: Resolving continuous flexibility and discrete heterogeneity from single particle cryo-EM. *J. Struct. Biol.* **213**, 107702 (2021).

54. Goddard, T. D. *et al.* UCSF ChimeraX: Meeting modern challenges in visualization and analysis. *Protein Sci.* **27**, 14–25 (2018).

55. Liebschner, D. *et al.* Macromolecular structure determination using X-rays, neutrons and electrons: recent developments in Phenix. *Acta Crystallogr. Sect. Struct. Biol.* **75**, 861–877 (2019).

56. Weis, D. *et al.* Biallelic Cys141Tyr variant of *SEL1L* is associated with neurodevelopmental disorders, agammaglobulinemia, and premature death. *J. Clin. Invest.* **134**, (2024).

57. Wang, H. H. *et al.* Hypomorphic variants of SEL1L-HRD1 ER-associated degradation are associated with neurodevelopmental disorders. *J. Clin. Invest.* **134**, (2024).

ARTICLE IN PRESS

ARTICLE IN PRESS

Acknowledgements

We thank the Jomaa, Shan, and Qi lab members for the helpful discussions. Cryo-EM data collection was conducted at the molecular electron microscopy core facility (RRID:SCR_019031) at the University of Virginia (UVA) School of Medicine which was built with NIH grant G20-RR31199. We thank Michael Purdy for assisting with the cryo-EM data collection and additional computational support. We thank Sarah Marks, Kinga Malezyna, and Travis Bishop for assisting with ribosome isolations, NAC purifications, and other biochemical assays. We also thank Shuangcheng Alivia Wu for initial help with preparation of *NACβ*-KO cells. This work was supported by NIH grant 1R35GM160490, the Owens Family Foundation, by the Searle Scholars Program, Grant #: SSP-2023-106, and aided by Grant # 134088-IRG-19-143-33-IRG from the American Cancer Society and the University of Virginia Comprehensive Cancer Center to A.J., by National Institutes of Health grant R35 GM136321 and National Science Foundation grant 2219287 to S.S., by National Institutes of Health grant R01DK120047, R01DK120330, R35GM130292 to L.Q. We acknowledge the cellular and molecular biology training program at UVA for support provided to E.M. through NIH T32GM139787-3 and the medical scientist training program for support provided to Z.J.L. In addition, the National Ataxia Foundation is acknowledged for support provided to L.L.L and Z.J.L through Post- and Pre-doctoral Fellowships NAF 918037 and 1036307, respectively.

Author Contributions

This study was conceived by A.J., S.S., E.M. and L.Q. Ribosomes were purified by E.M. and R.G. for structural and single molecule experiments, respectively. Y.P. provided materials used in various biochemical experiments throughout the study (site directed point mutagenesis, plasmid

ARTICLE IN PRESS

ARTICLE IN PRESS

preps, cultured cells for ribosome isolations and assisted with the NAC purifications). E.M. collected, processed cryo-EM data, and built the atomic model and assembled the structural snapshots. R.G. conducted the single molecule total internal reflection microscopy studies. L.L.L., L.E.Z., and Z.J.L. generated the *NACβ*-KO cells and conducted the cell-based experiments. A.J., S.S., and L.Q. supervised the work. E.M., A.J., S.S., and R.G. wrote the manuscript. All authors contributed to data analysis and the final version of the manuscript.

Competing Interests

The authors declare that they have no competing interests.

ARTICLE IN PRESS

ARTICLE IN PRESS

Figure Legends

Figure 1. Structure of NAC in complex with a ribosome translating a mitochondrial nascent chain. **A)** Cryo-EM structure of the OXA1L NAC-RNC$_{MTS}$ complex. The inset shows a closeup of NAC docked near the polypeptide exit tunnel (PET- red asterisk). Large ribosomal proteins are colored in cyan; small ribosomal proteins are colored in beige; NACβ is colored in green, and NACα is colored in orange; P-site tRNA and the nascent chain are colored pink; rRNA is colored in grey. **B)** Schematic of NAC bound near the PET. Created in BioRender. Maldosevic, E. (2026) https://BioRender.com/ory2nww. **C)** Interaction of the N-terminal fluke of NACβ with eL22 and H59, with the cryo-EM map shown as mesh. **D)** Interaction of NAC βh1, βh2, and the intervening linker with rRNA H59 and eL19. The cryo-EM map is shown as mesh. **E)** Side view of NAC βh2 contacts with eL19 and H59. **F)** Comparison of the NAC-RNC$_{MTS}$ model to the previously published model of ribosomes translating an ER signal sequence (NAC-RNC$_{SS}$, PDB 7QWR). Red arrows indicate the conformational change observed for the NAC barrel and H59. **G)** Rearrangement of H59 between the NAC-RNC$_{MTS}$ and NAC-RNC$_{SS}$ structure. Red arrows depict the conformational change of the bases G2706 and U2707 in the RNC$_{MTS}$ model (red), compared to the RNC$_{SS}$ model (blue).

ARTICLE IN PRESS

ARTICLE IN PRESS

Figure 2. Structural and biochemical analysis identifies a molecular switch in NACβ. **A)** Closeup of the residues in NAC βh2 and the preceding linker that mediate interactions with H59. The cryo-EM map is shown as a mesh. Sequence alignments below show the conservation of the highlighted residues/charge. **B)** Comparison of the conformational change in NACβ between the NAC-RNC_{MTS} structure and the NAC-RNC_{SS} (PDB 7QWR), depicted with an arrow. Dashed lines indicate distance for the movement of Lys42 and Arg35. **C, D)** Representative western blots showing the ribosome association of WT NAC and indicated mutants in the NAC switch region determined by the co-sedimentation assay. RPL10a was used as a loading control. Additional replicates used in the quantifications are shown in Supplementary Fig. 9C-D. Bar graphs below the blots show the quantification of NAC bands in the pellet relative to WT NAC (n=3). Values are plotted as Mean ± SD. Statistics: one-way ANOVA with Dunnett's multiple comparisons test (***p= 0.0003, ****p<0.0001). Source data are provided as a Source Data file.

ARTICLE IN PRESS

Figure 3. NAC molecular switch mutants impair barrel docking near the ribosome exit tunnel. **A)** NAC-RNC_{MTS} structure, with spheres depicting mutated NAC-ribosome contacts in the switch region used for single molecule experiments. FRET donor is indicated on the NAC barrel and the approximate position of the FRET acceptor is indicated on the nascent chain. **B)** Schematic representation of the smTIRFM experiment to define NAC barrel dynamics on the ribosome. Created in BioRender. Maldosevic, E. (2026) https://BioRender.com/f3oog5p. OXA1L RNC_{MTS} was immobilized on quartz slides. FRET efficiency between a donor dye (green star) in the NAC barrel and an acceptor dye (red star) on the nascent chain measures NAC barrel docking at the polypeptide exit tunnel (PET). **C)** Representative smFRET traces of NAC interacting with OXA1L RNC_{MTS}. Left panels show the acceptor (red) and donor (green) emission intensity when the donor is excited. Right panels show the corresponding FRET traces (cyan) and Hidden Markov Modeling (HMM) of the data (orange lines) to establish the number of states and their mean FRET values. Dashed black lines indicate acceptor bleaching, while grey indicates the data after donor bleaching; both are excluded from further data processing. **D)** smFRET histograms for wild-type NAC (grey) and mutants $NAC_{HR:AA}$ (left; magenta) and $NAC_{KF:AA}$ (right, blue). PDF, probability density function. 'N', number of measurements. The solid lines show the fit of data to the sum of three Gaussian functions with low, medium, and high mean FRET values, and dotted lines show the constituent Gaussian components. **E**) Summary of the distribution of WT and mutant NAC in the different FRET states. Source data are provided as a Source Data file.

ARTICLE IN PRESS

Figure 4. The MTS drives stable binding of the NAC barrel adjacent to the ribosome exit tunnel. **A**) Scheme showing the MTS mutations in the OXA1L nascent chain. 'aMTS' (*dark blue*) denotes the amphiphilic N-terminal helix in the nascent chain, the rest of the presequence is in *light blue*. 'SS' denotes the hydrophobic core of the ER signal sequence from preprolactin (LLLLLLVSNLLLCQGVVST). The FRET acceptor was positioned 35 amino acids from the C-terminus in all nascent chains tested (red star). The gray box denotes the approximate span of residues located within the ribosomal exit tunnel. **B**) smFRET histograms for NAC bound to ribosomes displaying $OXA1L_{\Delta MTS}$ (left panel) and $OXA1L_{MTS\text{-}to\text{-}SS}$ (right panel), using the same FRET pair as in Figure 3. The dashed line shows the data for wildtype OXA1L RNCs for comparison. N, number of FRET events used to construct the histogram. PDF, probability density function. The data were fit to the sum (solid lines) of three Gaussian functions (dashed lines). **C**) Summary of the distribution of NAC in different FRET states, from analysis of the data in (B). **D**) Kinetics of NAC dissociation from the indicated RNCs. The lines show fits of the data to a double exponential function, which gave the indicated dissociation rate constants for the fast- (k_{fast}) and slow- (k_{slow}) dissociating populations. Grey dashed lines show the data with WT RNC_{MTS} for comparison. Number of FRET time traces used for establishing kinetic parameters was 58 for OXA1L WT group, 92 for $OXA1L_{\Delta MTS}$ and 70 for $OXA1L_{MTS\text{-}to\text{-}SS}$. **E**) Summary of the fraction of slow-dissociating population of NAC bound to the indicated RNCs. From fits to the data in (D). Values are shown as fitted parameter ± standard error (SE) of the fit. **F**) Close-up of the NAC barrel conformations on ribosomes translating $OXA1L_{\Delta MTS}$. Cryo-EM maps filtered to 8Å are overlayed showing the NAC barrel in the H59-docked (green) and shifted H59-undocked conformation (purple). Source data are provided as a Source Data file.

ARTICLE IN PRESS

ARTICLE IN PRESS

Figure 5. NAC molecular switch mutants fail to regulate SRP activation on the ribosome and lead to elevated ER-stress in human cells. **A)** Surface model depicting the overlap between SRP (PDB 7QWQ) and NAC (this study) on the ribosome. **B)** Scheme depicting the smTIRFM experiments to measure the conformational distribution of SRP on the ribosome. Created in BioRender. Maldosevic, E. (2026) https://BioRender.com/n47hfd6. RNCs were immobilized on quartz slides. FRET was measured between a donor dye (green star) on SRP19 and an acceptor dye (red star) on the SRP54 NG domain. High FRET efficiency was observed when SRP is in the targeting active proximal conformation (left) and correlates with SRP-SRP receptor interaction rates[43]. **C, D)** smFRET histograms of SRP bound to ribosomes translating nascent chains containing an ER signal sequence (C) and an MTS (D), with or without the indicated NAC variant. PDF, probability density function. 'N' indicates the number of measurements. The data were fit to the sum (solid line) of two or three Gaussian functions (dashed lines), with the mean FRET value of each Gaussian indicated. **E)** Summary of the effect of WT and mutant NAC on the conformation of SRP bound to ribosomes translating ER (RNC_{SS}) and mitochondrial nascent chains (RNC_{MTS}). **F, G)** Experiments to measure ER stress in *NACβ* knockout (KO) HEK293T cells, with or without transient overexpression of the indicated NAC variant. ER stress is measured by monitoring the expression of BiP and PDI protein (F) and levels of spliced (s) and unspliced (u) *XBP1* mRNA (G). HSP90 and *L32* are loading controls used for the WB and RT-PCR gels, respectively. The percentage of the ratio of spliced to total *XBP1* shown below the gel. The bar graphs in (F) ($n = 6$) and (G) ($n = 3$) show the quantification of the blots and gels from individual biological replicates normalized to controls. Representative blots and gels are depicted. Arb, arbitrary units. Values are plotted as mean ± SEM. Statistics: *$p < 0.05$, **$p < 0.01$, ***$p < 0.001$ and ****$p < 0.0001$ by one-way ANOVA followed by Dunnett's multiple comparisons test. EV- empty vector. Source data are provided as a Source Data file, with P values listed.

ARTICLE IN PRESS

ARTICLE IN PRESS

Figure 6. Model for MTS sensing by the NAC switch on translating ribosomes. NAC binds to all translating ribosomes using the NAC anchor (I). The NAC barrel domain can additionally dock near the polypeptide exit tunnel (PET), which is destabilized by hydrophobic ER signals, allowing SRP to engage the nascent chain and target the ribosome to the ER membrane (IIA). On MTS-containing ribosomes, the NAC molecular switch docks the barrel domain at H59 following a conformational change in H59. This prevents the mistargeting of mitochondrial proteins by SRP and enables their subsequent sorting to the mitochondria (IIB). Created in BioRender. Maldosevic, E. (2026) https://BioRender.com/hqggri6.

ARTICLE IN PRESS

ARTICLE IN PRESS

Editor's Summary

How ribosome-bound NAC distinguishes mitochondrial precursors from ER clients has remained unclear. Here, authors reveal a molecular switch in NAC that limits SRP access to nascent mitochondrial precursors and prevents their mistargeting to the ER.

Peer review information: *Nature Communications* thanks Andrei Korostelev, and the other, anonymous, reviewer(s) for their contribution to the peer review of this work. A peer review file is available.

ARTICLE IN PRESS

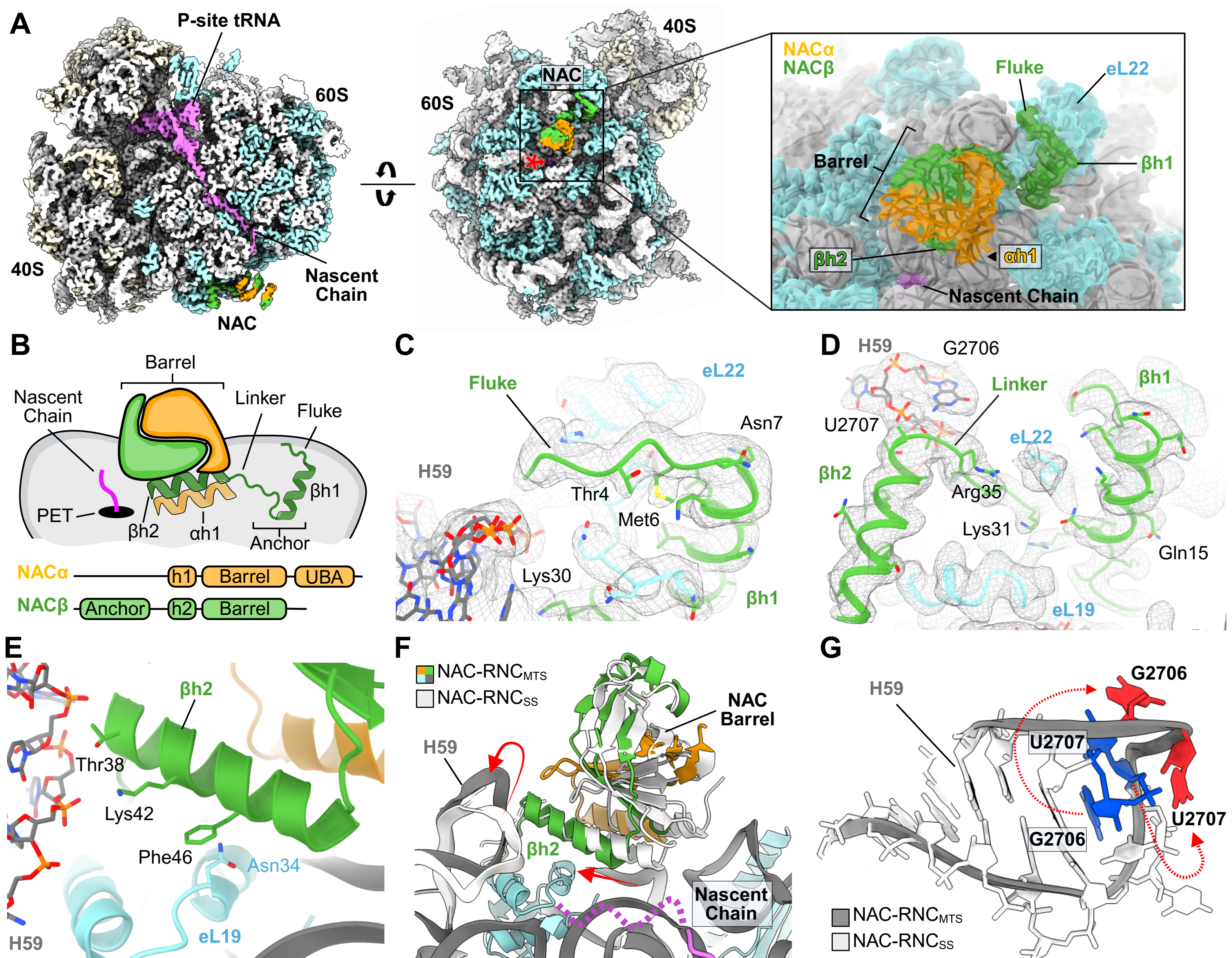
A
P-site tRNA
60S
40S
Nascent Chain
NAC
40S
NAC
60S
NACα
NACβ
Fluke
eL22
Barrel
βh1
βh2
αh1
Nascent Chain
B
Barrel
Nascent Chain
Linker
Fluke
βh1
PET
βh2
αh1
Anchor
NACα
h1
Barrel
UBA
NACβ
Anchor
h2
Barrel
C
Fluke
eL22
Asn7
H59
Thr4
Met6
Lys30
βh1
D
H59
G2706
Linker
βh1
U2707
eL22
βh2
Arg35
Lys31
Gln15
eL19
E
βh2
Thr38
Lys42
Phe46
Asn34
H59
eL19
F
NAC-RNC_{MTS}
NAC-RNC_{SS}
NAC Barrel
H59
βh2
Nascent Chain
G
H59
G2706
U2707
U2707
G2706
NAC-RNC_{MTS}
NAC-RNC_{SS}

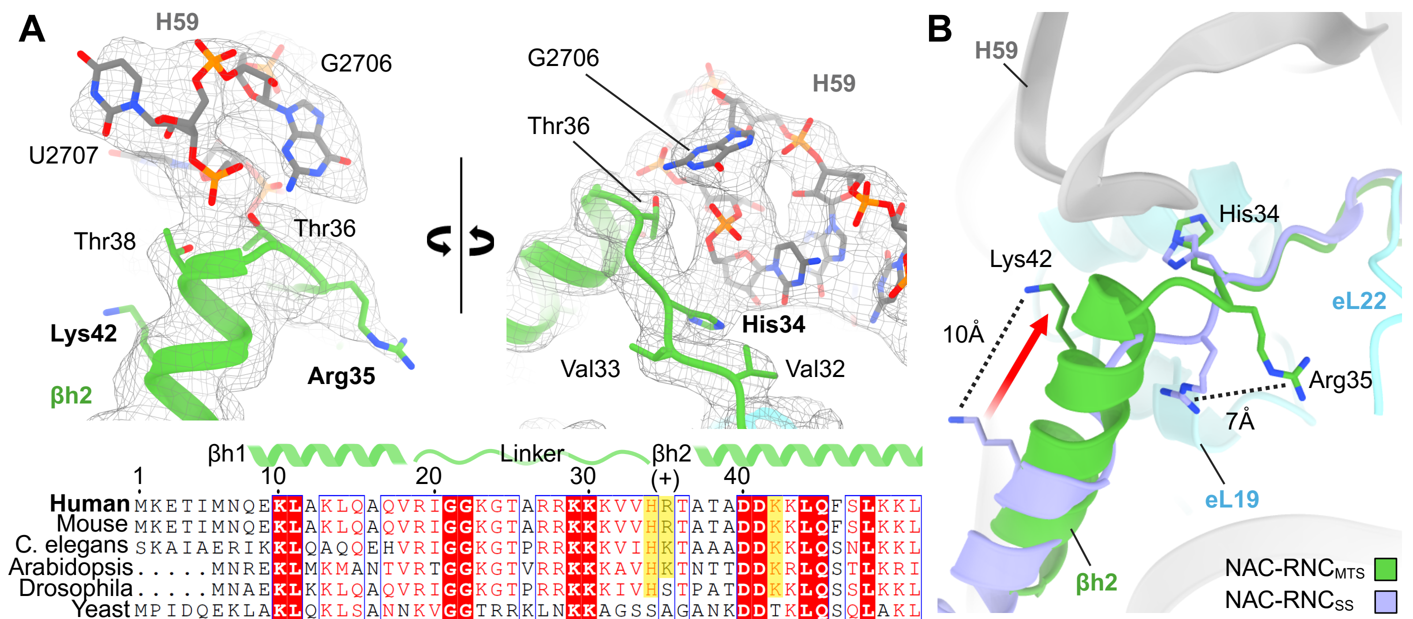

A
H59
G2706
U2707
Thr38
Thr36
Lys42
βh2
Arg35
Thr36
His34
Val33
Val32
B
H59
His34
Lys42
10Å
eL22
Arg35
7Å
eL19
βh2
NAC-RNCMTS
NAC-RNCSS
βh1
Linker
βh2
(+)
Human
Mouse
C. elegans
Arabidopsis
Drosophila
Yeast

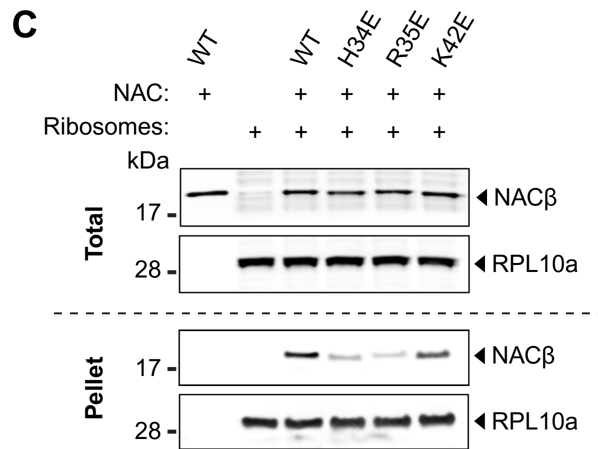

C
WT
WT
H34E
R35E
K42E
NAC:
Ribosomes:
kDa
Total
Pellet
17
28
NACβ
RPL10a

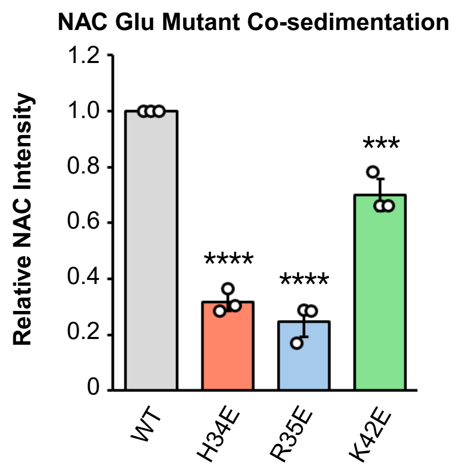

NAC Glu Mutant Co-sedimentation
Relative NAC Intensity
1.2
1.0
0.8
0.6
0.4
0.2
0
****
****
***
WT
H34E
R35E
K42E

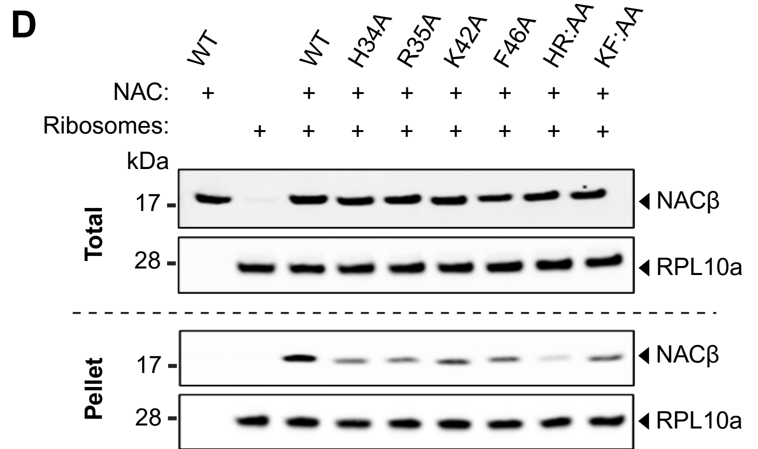

D
WT
WT
H34A
R35A
K42A
F46A
HR:AA
KF:AA
NAC:
Ribosomes:
kDa
Total
Pellet
17
28
NACβ
RPL10a

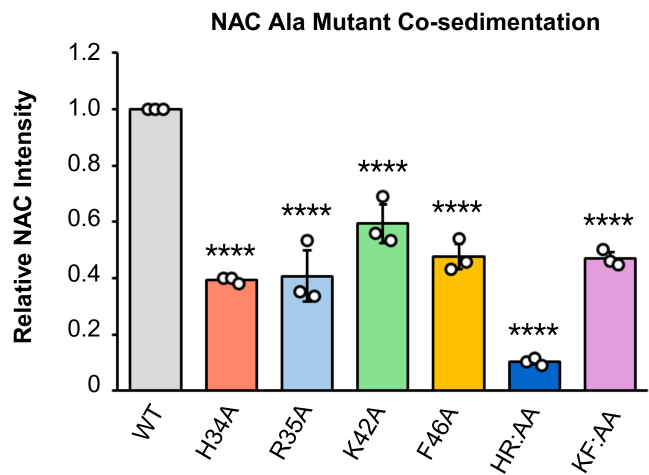

NAC Ala Mutant Co-sedimentation
Relative NAC Intensity
1.2
1.0
0.8
0.6
0.4
0.2
0
****
WT
H34A
R35A
K42A
F46A
HR:AA
KF:AA

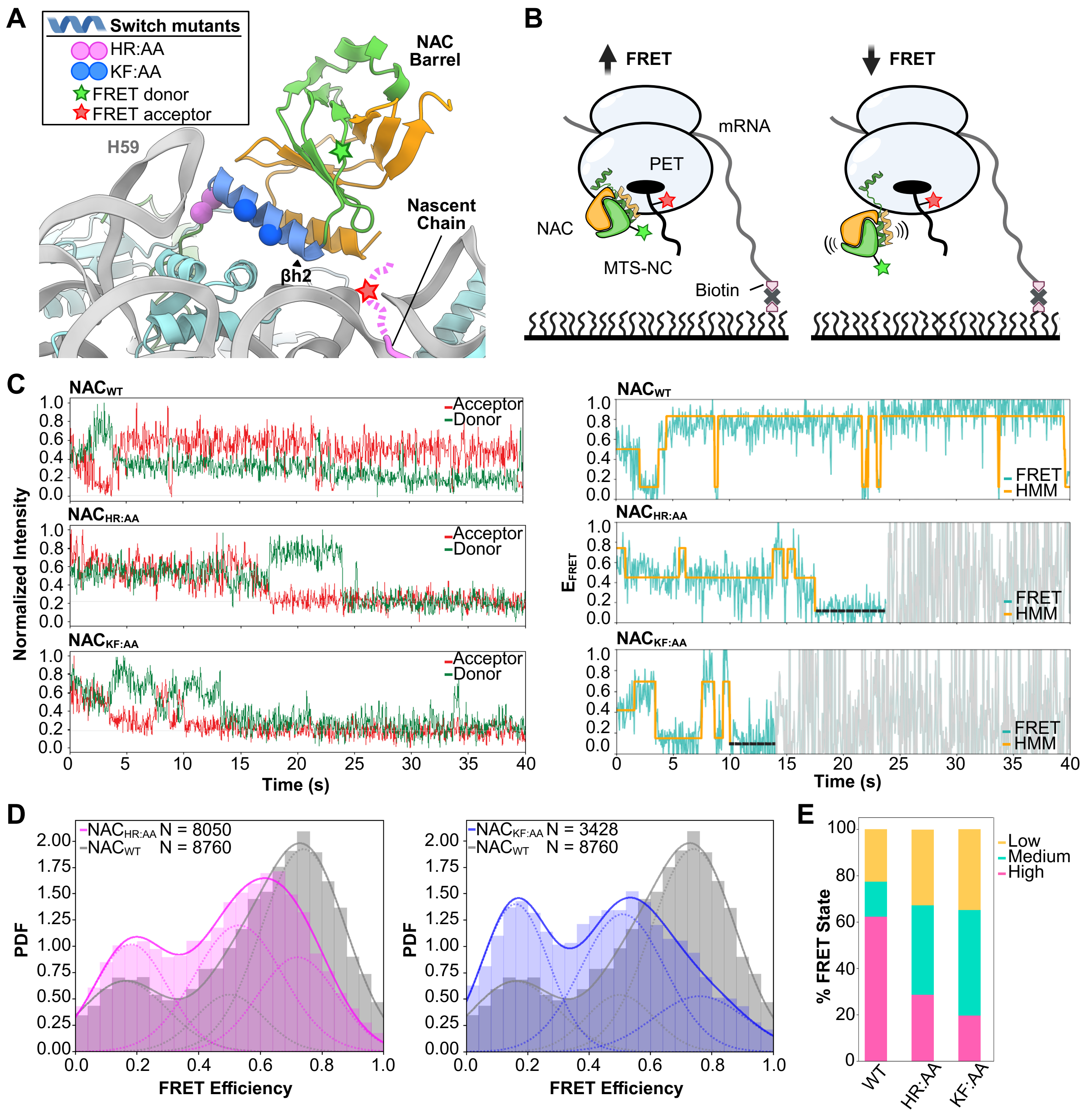
A
Switch mutants
HR:AA
KF:AA
FRET donor
FRET acceptor
H59
NAC
Barrel
Nascent
Chain
βh2
B
FRET
FRET
mRNA
PET
NAC
MTS-NC
Biotin
C
NACWT
NACHR:AA
NACKF:AA
Acceptor
Donor
Normalized Intensity
Time (s)
EFRET
FRET
HMM
D
NACHR:AA N = 8050
NACWT N = 8760
NACKF:AA N = 3428
PDF
FRET Efficiency
E
% FRET State
Low
Medium
High
WT
HR:AA
KF:AA

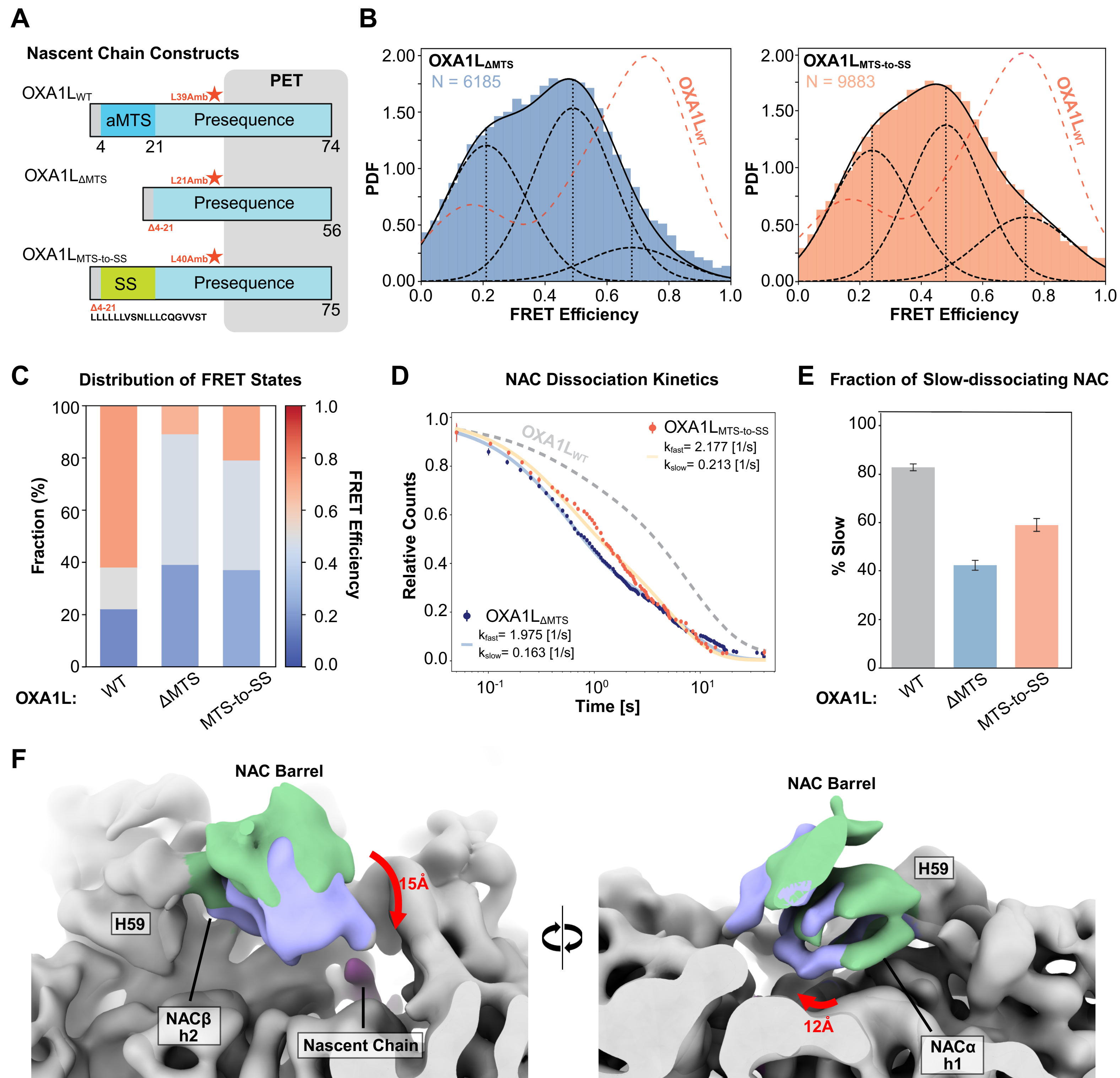

A
Nascent Chain Constructs
PET
OXA1LWT
L39Amb
aMTS
Presequence
4
21
74
OXA1LΔMTS
L21Amb
Presequence
Δ4-21
56
OXA1LMTS-to-SS
L40Amb
SS
Presequence
Δ4-21
LLLLLLVSNLLLCQGVVST
75
B
OXA1LΔMTS
N = 6185
OXA1LWT
PDF
FRET Efficiency
OXA1LMTS-to-SS
N = 9883
OXA1LWT
PDF
FRET Efficiency
C
Distribution of FRET States
Fraction (%)
FRET Efficiency
OXA1L:
WT
ΔMTS
MTS-to-SS
D
NAC Dissociation Kinetics
OXA1LWT
OXA1LMTS-to-SS
kfast= 2.177 [1/s]
kslow= 0.213 [1/s]
OXA1LΔMTS
kfast= 1.975 [1/s]
kslow= 0.163 [1/s]
Relative Counts
Time [s]
E
Fraction of Slow-dissociating NAC
% Slow
OXA1L:
WT
ΔMTS
MTS-to-SS
F
NAC Barrel
H59
15Å
NACβ
h2
Nascent Chain
NAC Barrel
H59
12Å
NACα
h1

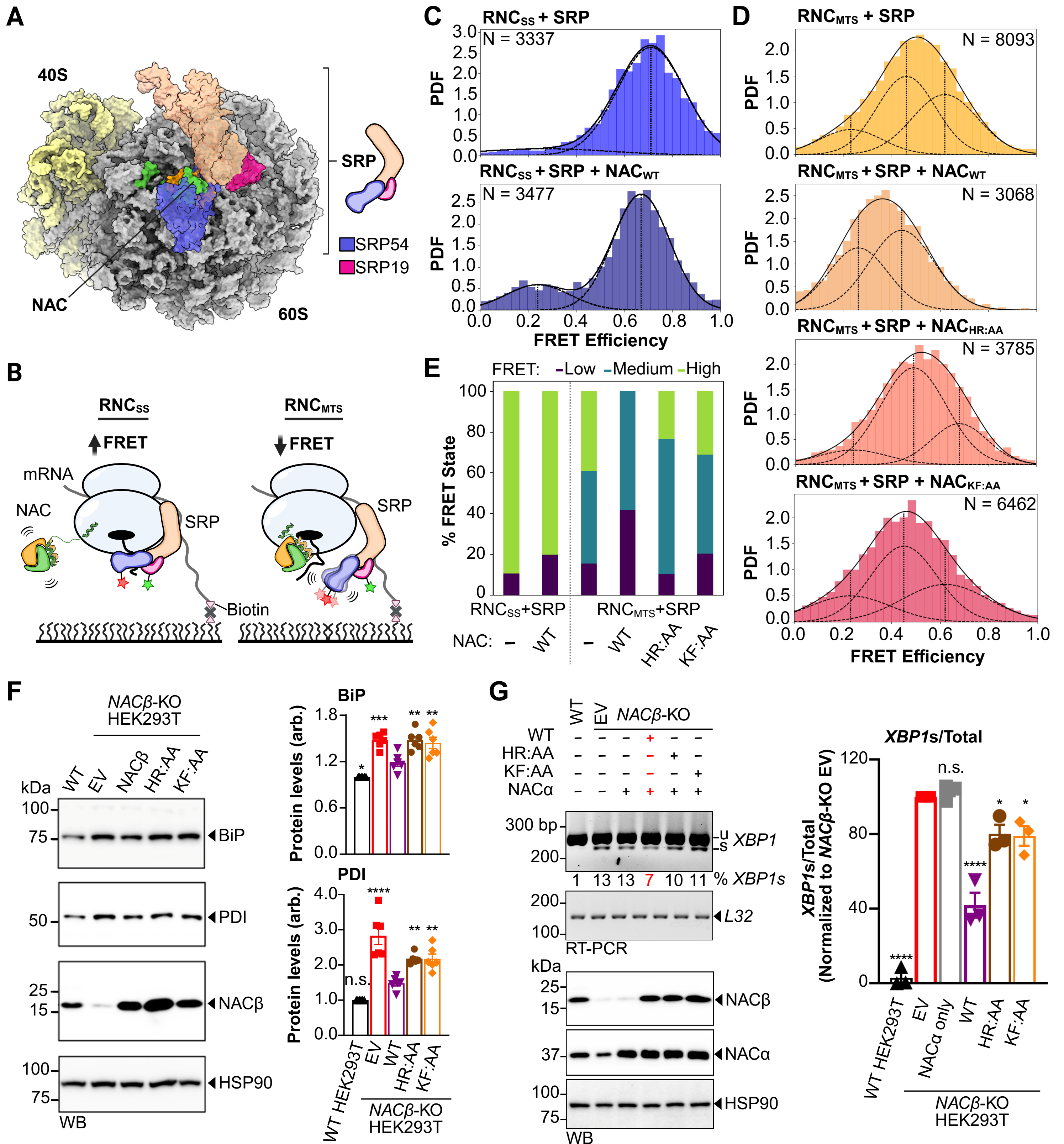
A
40S
SRP
SRP54
SRP19
NAC
60S
B
RNCSS
FRET
RNCMTS
FRET
mRNA
NAC
SRP
Biotin
C
RNCSS + SRP
N = 3337
RNCSS + SRP + NACWT
N = 3477
PDF
FRET Efficiency
D
RNCMTS + SRP
N = 8093
RNCMTS + SRP + NACWT
N = 3068
RNCMTS + SRP + NACHR:AA
N = 3785
RNCMTS + SRP + NACKF:AA
N = 6462
FRET Efficiency
E
FRET: Low Medium High
% FRET State
RNCSS+SRP
RNCMTS+SRP
NAC: – WT – WT HR:AA KF:AA
F
NACβ-KO HEK293T
WT EV NACβ HR:AA KF:AA
kDa
BiP
PDI
NACβ
HSP90
WB
BiP
PDI
Protein levels (arb.)
n.s.
WT HEK293T EV WT HR:AA KF:AA
NACβ-KO HEK293T
G
WT EV NACβ-KO
WT
HR:AA
KF:AA
NACα
300 bp
u
s
XBP1
1 13 13 7 10 11 % XBP1s
L32
RT-PCR
kDa
NACβ
NACα
HSP90
WB
XBP1s/Total
XBP1s/Total (Normalized to NACβ-KO EV)
n.s.
WT HEK293T EV NACα only WT HR:AA KF:AA
NACβ-KO HEK293T

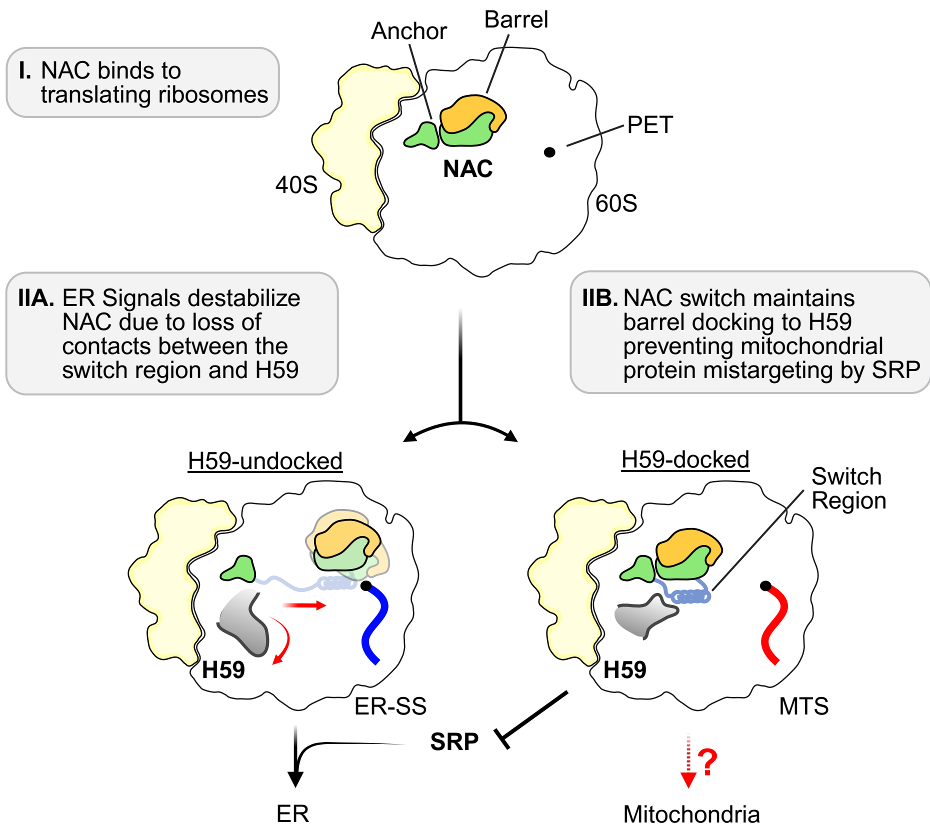
I. NAC binds to translating ribosomes
Anchor
Barrel
PET
NAC
40S
60S
IIA. ER Signals destabilize NAC due to loss of contacts between the switch region and H59
IIB. NAC switch maintains barrel docking to H59 preventing mitochondrial protein mistargeting by SRP
H59-undocked
H59-docked
Switch Region
H59
H59
ER-SS
MTS
SRP
?
ER
Mitochondria